Version: Accepted Version

---

**Article:**

Allulakshmi, K, Vinod, JS, Heitor, A et al. (2022) Numerical Modeling of Cone Penetration Test: An LBM–DEM Approach. International Journal of Geomechanics, 22 (8). ISSN: 1532-3641

https://doi.org/10.1061/(ASCE)GM.1943-5622.0002497

---

# Numerical modeling of cone penetration test: A LBM - DEM approach

*Krishna Allulakshmi*[1], *Jayan S. Vinod*[1*], *Ana Heitor*[2], *Andy Fourie*[3]

[1]Faculty of Engineering and Information Sciences, University of Wollongong, NSW 2522, Australia.

[2]Faculty of Engineering and Physical Sciences, University of Leeds, Leeds LS@ 9DY, UK

[3]Faculty of Engineering and Mathematical Sciences, University of Western Australia, WA 6009, Australia.

## Abstract

In this paper, the Discrete Element Method (DEM) is coupled with the Lattice Boltzmann Method (LBM) to model the cone penetration test of saturated granular media. The coupled numerical model was calibrated using one-dimensional consolidation theory. The results obtained from the 1D consolidation test simulation showed good agreement with the analytical equation proposed by Terzaghi. A series of LBM-DEM simulations were then carried out to understand the effect of penetration rate on the behavior of saturated granular materials during the cone penetration test. The model has predicted a significant influence on the excess pore fluid pressure and an insignificant influence on the cone resistance responses and has qualitatively captured the effect of penetration rate consistent with the experimental data. The simulation results showed that excess pore fluid pressure increased with an increase in penetration rate. The particle displacement and fluid velocity contours have provided insights into the particle behavior and fluid pressure fluctuations during CPT. The increase in excess pore fluid pressure has been attributed to the fluid pressure gradients created by the cone in the fluid system based on the penetration rate. The pore pressure distribution plots have shown a maximum pore fluid pressure below the cone region and over the cone shoulder position. A consistent evolution pattern of fabric anisotropy has been observed throughout the depth in all the penetration rate conditions. The fabric components $(\emptyset_{22})$ and $(\emptyset_{11})$ have dominated around the cone area and at the boundary region, respectively. This indicates the preferential orientation of contacts in the vertical direction at the cone region and the horizontal direction at the boundary region. The simulation results have demonstrated that the LBM-DEM model can efficiently simulate the cone penetration test and associated pore fluid pressure, including the cone-particle-fluid interactions during CPT.

**Keywords:** Discrete Element Method, Lattice-Boltzmann method, 1D consolidation test, Cone resistance, Excess pore pressure.

# Introduction

The cone penetration test (CPT) is an in-situ test widely used in geotechnical engineering for investigating soil characteristics and associated mechanical properties. Analyzing the engineering soil properties based on CPT has become standard due to its reliability, repeatability, and accuracy (Lunne et al. 2002). The CPT is fast and provides continuous information on soil profile, capturing the proportion and variability of soil layers. It is also operator independent and cost effective. In contrast, the CPT test is not suitable for penetration into hard materials like gravels or cemented materials, no possible recovery of the soil sample, and precise calibration of the equipment is required before testing (Ramsey 2010). Nevertheless, the fundamental advantages of CPT outweigh the disadvantages; hence it is extensively used in the geotechnical classification of the soil.

The CPT test investigation mainly reports cone resistance ($q_t$), frictional sleeve resistance ($f_s$), pore pressure response ($u$) and shear wave velocity of the soil. These results can be collectively used to assess the soil properties (Lunne et al. 2002). The CPT test can be performed on different soils (e.g., soft clays to sands) at a standard penetration rate of $20 \pm 5$ mm/s (ASTM International 2012). While using the standard penetration rate, different drainage conditions are encountered depending on soil type and its permeability (Kim et al. 2008). For instance, the standard penetration rate creates an undrained condition for clayey soils and drained conditions for clean sands. In comparison, a partially drained condition prevails for mixtures of clay, silt and sand (Yi et al. 2012; DeJong and Randolph 2012). The influence of penetration rate on the different types of soils (e.g., clays, silts and mixture of clay & sand, silt & sand) has been investigated in several past studies through centrifuge model and calibration chamber tests (e.g., Randolph and Hope 2004; Schneider et al. 2007; Kimm et al. 2008; Jaeger et al. 2010; Mahmoodzadeh et al. 2011). In addition, researchers have also carried out numerical modeling studies to understand the effect of penetration rate on soils using the Finite Element Model (e.g., Obzrud et al. 2011; Yi et al. 2012; Sheng et al. 2014; Suzuki 2015). The results showed that a decrease in penetration rate causes a change in drainage condition, which leads to the increase of cone resistance and decrease of pore pressure.

Over the past years, researchers have studied the penetration rate effect on CPT in the sand through in-situ and laboratory testing (e.g., Dayal and Allen 1975; Chapman 1979; Juran and Tumay 1989; Van der Poel and Schenkeveld 1998; Silva and Bolton 2004). The majority of the studies have considered the penetration rate in the range of 0.4 mm/s to 20 mm/s. However, Pournaghiazar et al. (2013) and Kluger et al. (2021) have reported no excess pore water pressure in the sand at a standard penetration rate of 20 mm/s. This may be due to the dissipation of excess pore water pressure because of the high permeability nature and adopted drained boundary conditions. Nevertheless, Dayal and Allen (1975) and Juran and Tumay (1989) have conducted CPT studies having penetration rates ranging from 1.3 – 811.4 mm/s and 2 -100 mm/s, respectively. The studies have all demonstrated that penetration rate has an insignificant influence on cone resistance in the case of clean sands.

Juran and Tumay (1989) conducted in-situ tests to study the penetration rate effect on stratified soil where the saturated sand was present between two clay layers. They found that the pore pressure increased with the rate of penetration. The recorded pore pressures approach the hydrostatic pressure $u_0$ at a penetration rate of 2 mm/s, but pore pressures generated at a penetration rate of 100 mm/s exceed four times $u_0$. This indicates that drained condition prevailed at 2 mm/s, while partially drained or undrained condition behavior occurred at 100 mm/s. Their study highlights that in a stratified soil system, when a loose sand layer is present between two clayey soils, the drainage conditions near sand layer boundaries considerably diminish the dissipation rate. It can be understood that pore water pressure response in such sand seams is much different from that measured in thick layers of identical sands with the same relative density. Under such circumstances, sand may be subjected to undrained conditions leading to the development of excess pore pressure during loading.

So far, limited experimental research work has been carried out on sands to investigate the influence of penetration rate on the pore pressure generation during CPT (Silva and Bolton 2004; Juran and Tumay 1989). While the experimental results at high penetration rates are scarce, the effect of high penetration rates in clean sands in a saturated state is examined herein with numerical simulations. Therefore, this study simulates the excess pore pressure generation in the sand for different cone penetration rates in fully undrained conditions using a fluid coupled discrete mechanics model.

The Lattice Boltzmann Method (LBM) is a numerical technique that solves the Boltzmann equation based on the kinetic theory with the fluid particle distribution functions. The Boltzmann equation is considered an approximation of the incompressible Navier-Stokes equations (Timm et al. 2016). In LBM, the fluid behavior is modeled at the mesoscale (i.e., at the soil-pores scale level), and the fluid variables such as fluid pressure, fluid velocity are obtained at the soil pores. The coupled LBM-DEM model simulates fluid flow at the pore-scale level and soil behavior at the particle level representing the interactions between the pore-fluid and the soil particles. In this study, the LBM is coupled with DEM using the Immersed Moving Boundary (IMB) method, enforcing a no-slip boundary condition at the fluid-soil particle interface using the non-equilibrium bounce-back principle.

Recently, the coupled LBM-DEM model has been used to model many engineering problems (e.g., sand production in borehole, piping, liquefaction, soil erosion) (e.g., Cook et al. 2004; Feng et al. 2007; Owen et al. 2011; Han and Cundall 2013; Cui et al. 2014; El Shamy and Abdelhamid 2014; Johnson et al. 2017; Yang et al. 2019; Indraratna et al. 2021). Feng et al. (2007) incorporated the turbulence model into LBM and simulated particle transportation during high Reynolds number flows. Boutt et al. (2011) simulated sand production in different viscous fluid wells and investigated the effect of particle shape friction coefficient on production rate. Johnson et al. (2017) simulated a 2D undrained biaxial test under confined loading using the LBM-DEM model and compared the response with constant volume simulation using DEM. Yang et al. (2019) simulated the collapse of a densely packed 3D granular column in water and compared the granular flow-free surface results with experiments. Although, LBM-DEM numerical method is widely used in geomechanics, there are generic limitations/issues such as stability of the model, implementation of boundary conditions. These issues must be precisely dealt with while employing the model to ensure an accurate simulation. To achieve a stable incompressible flow simulation in LBM, the fluid's Mach number ($M_a = \boldsymbol{U}/c_s$) must always be less than 0.1. Maintaining this condition in a coupled simulation can be challenging, where the rapid movement of particles is present (e.g., simulation of liquefaction problems). Moreover, modeling the testing chamber boundaries of any arbitrary shape requires the development and integration of additional subroutines. For instance, to implement the boundary conditions (no-slip) for a flexible cylindrical geometry (triaxial test chamber) involves continuous recording of boundary nodes for every LBM timestep. Incorrect tracking of node positions will lead to a mismatch of LBM - DEM defined physical boundaries and may impart an inaccurate fluid force on particles.

The Discrete Element Method (DEM) developed by Cundall and Strack (1979) is an alternative to the continuum mechanics approach. It enables a better understanding of complex macroscopic material response through particle level micromechanics (e.g., contact density, contact force distribution, particle displacements). The macroscopic behavior of granular material obtained from DEM simulations are predominantly influenced by the particle level input parameters such as inter-particle friction ($\mu$), particle young's modulus ($E^*$) and particle shape (Sitharam and Vinod 2010; O'Sullivan 2011; Yang et al. 2012; Senetakis et al. 2012, 2013; Huang et al. 2014; Kasyap and Senetakis 2019). These parameters have a significant impact on the strength and volume change behavior of granular materials during shear loading. The typical particulate features of the soil such as surface roughness, shape angularity can be incorporated into the model through the input parameters (Otsubo et al. 2017; Nadimi et al. 2019; Mollon et al. 2020; Reddy et al. 2022). As the particle level contact stiffness in normal and shear directions are directly controlled by particle young's modulus, utmost importance should be given while choosing the material input parameters for simulating the bulk soil behavior. Researchers have employed DEM to simulate CPT on dry soils to analyze the soil behavior from individual particle-scale to the macroscopic scale (e.g., Huang et al. 1994; Jiang et al. 2006; Kinloch and O'Sullivan 2007; Arroyo et al. 2011; Mcdowell et al. 2012; Butlanska et al. 2013; Jiang et al. 2014 Falagush et al. 2015; Ciantia et al. 2016; Ecemis and Bakunowicz 2018; Khosravi et al. 2019). Jiang et al. (2006) modeled a 2D CPT using DEM to investigate the effect of interface friction between cone-soil under plane strain conditions. Arroyo et al. (2011) and Butlanska et al. (2013) developed a three-dimensional Virtual Calibration Chamber (VCC) model with spherical particles and examined the CPT results at various particle scale levels. They studied the influence of key parameters on penetration resistance (e.g., relative density, boundary conditions, particle rotation). McDowell et al. (2012) and Falagush et al. (2015) have studied the effect of particle shape and particle crushing on cone penetration testing (CPT). Their study adopted a particle refinement method to incorporate realistic particle size and reduce computational time. Their particle crushing model depicted a significant reduction in the cone resistance compared to the non-crushing model. Ciantia et al. (2016) investigated the effect of particle crushing during CPT with crushable microporous discrete material. They identified that the initial approximation of internal porosity variation in particle diameter considerably affects crushing.

It is understood that all the studies on DEM modeling of CPT were performed on dry soils, and no research study has been reported on the modeling of CPT test on saturated soils by incorporating the fluid. While in the past studies, researchers have successfully implemented the LBM-DEM coupled model to analyze different geotechnical problems (e.g., Cook et al. 2004; Feng et al. 2007). However, the development of excess pore pressure and its evolution behavior were not captured during shearing. This is critical to adequately model the cone penetration process. In this study, the coupled LBM-DEM model is employed to capture the excess pore pressure generation and obtain a detailed insight into the micromechanical behavior during the CPT test at various penetration rates. The novel application of this coupled model allows modeling the soil particles at microscale and fluid flow at the pore-scale level, which is essential for large deformations problems such as cone penetration test.

## Numerical method

### Lattice Boltzmann method

LBM is a mesoscale fluid solver used for modeling fluid governed by Navier–Stokes equation (Cook et al. 2004). In LBM, the entire fluid system is modeled as packets of particles (mass), which can move about a predefined regular lattice or grid. The time and spatial evolution of fluid is quantified by the particle distribution function with defined directions towards adjacent lattice nodes and its notation is given as $f_i(\boldsymbol{x}, t)$. The governing equation in LBM is defined with a single relaxation time approximation and a linearized BGK (Bhatnagar- Gross-Krook) collision operator (Bhatnagar et al. 1954), as follows:

$$f_i(\boldsymbol{x} + \boldsymbol{e}_i t, t + \Delta t) = f_i(\boldsymbol{x}, t) - \frac{1}{\tau}\left(f_i(\boldsymbol{x}, t) - f_i^{eq}(\boldsymbol{x}, t)\right) \tag{1}$$

where, $f_i(\boldsymbol{x}, t)$ is the fluid particle distribution function with discrete velocity set $\boldsymbol{e}_i$ at a lattice node located at position $\boldsymbol{x}$ for a given time $t$, $\tau$ is dimensionless relaxation time, $\Delta t$ denotes the time step. In LBM, at each time step fluid motion is solved in two phases, i.e., 'collision' and 'streaming' phases. The second term in the right-hand side of Eq. (1) represents a collision phase where the fluid mass streamed from all possible directions interacts and relaxes towards the equilibrium distribution function $f_i^{eq}(\boldsymbol{x}, t)$. The left-hand side of Eq. (1) represents the streaming phase where the calculated distribution is streamed from one lattice node to another node (say from $\boldsymbol{x}$ to $\boldsymbol{x} + \Delta x$). These operations are completed over an LBM time step $\Delta t$.

$f_i^{eq}(\boldsymbol{x}, t)$ is the local equilibrium distribution function for the fluid, based on the Maxwell distribution function (Timm et al. 2016):

$$f_i^{eq} = \rho w_i \left[ 1 + \frac{\boldsymbol{e}_i \cdot \boldsymbol{U}}{c_s^2} + \frac{(\boldsymbol{e}_i \cdot \boldsymbol{U})^2}{2c_s^4} - \frac{\boldsymbol{U}^2}{2c_s^2} \right] \tag{2}$$

where, $w_i$ is a weighting factor associated with $\boldsymbol{e}_i$ , $\rho$ is the fluid density, $\boldsymbol{U}$ is fluid velocity vector, the lattice speed of sound $c_s = 1/\sqrt{3}$. In this paper, the 2D regular lattice is shown in Fig. 1(a) was used to model the fluid phase. The discrete velocity set and the weighing factors of the lattice cell are given below:

$$\vec{e}_i = \begin{bmatrix} 1 & 1 & 1 & 0 & 0 & 0 & -1 & -1 & -1 \\ 1 & 0 & -1 & 1 & 0 & -1 & 1 & 0 & -1 \end{bmatrix} \tag{3}$$

$$w_i = \begin{cases} {}^{4}\!/_{9}, & i = 4. \\ {}^{1}\!/_{9}, & i = 1,3,5,7. \\ {}^{1}\!/_{36}, & i = 0,2,6,8. \end{cases} \tag{4}$$

Once the particle distribution function is obtained, the macroscopic fluid density $\rho$ and velocity $\boldsymbol{U}$ are computed at every lattice node from the distribution functions:

$$\rho = \sum_{i=0}^{8} f_i \tag{5}$$

$$\boldsymbol{U} = \frac{1}{\rho}\sum_{i=0}^{8} f_i\, \boldsymbol{e}_i \tag{6}$$

The fluid pressure is then calculated from the obtained fluid density using the equation of state (Timm et al. 2016):

$$P = \rho c_s^2 \tag{7}$$

Using multiscale Chapman-Enskog expansion (He and Luo 1997), the incompressible Navier-Stokes equations can be recovered, and a relationship is established for fluid kinematic viscosity $\vartheta$ involving relaxation time $\tau$, fluid time step $\Delta t_{LBM}$ and lattice spacing $\Delta x$ :

$$\vartheta = c_s^2(\tau - 0.5)\frac{\Delta x^2}{\Delta t_{LBM}} \tag{8}$$

The fluid time step is determined from Eq. (8) and is dependent on kinematic viscosity $\vartheta$, lattice spacing $\Delta x$, relaxation time $\tau$ (model constant). In LBM, the simulation of incompressible flow is feasible at low Mach number ($M_a = \boldsymbol{U}/c_s$) only, where the Mach number should be less than 0.1. The numerical stability of LBM simulation is mainly associated with the relaxation time parameter, which determines fluid compressibility in LBM applications. The fluid compressibility relation is as follows (Johnson et al. 2017):

$$\beta = 1/\rho c_s^2 \tag{9}$$

### Immersed moving boundary method

In this study, the immersed moving boundary (IMB) method proposed by Noble and Torczynski (1998) based on the non-equilibrium bounce back function is used to capture fluid-solid interactions at the particle interface. This method enables an efficient coupling framework and allows the soil media to move across the fluid grid (Zou and He 1997; Timm et al. 2016). To monitor the volume fraction occupancy of lattice cells by solids, a special parameter $\varepsilon_s$ is introduced. The range of $\varepsilon_s$ lies between 0 and 1. Where, $\varepsilon_s = 1$ represents cell completely inside the solid boundary and $\varepsilon_s = 0$ represents cell is free from solid occupancy, and for $0 < \varepsilon_s < 1$ the cell is partially filled with solid presence. Based on the volume fraction occupancy and relaxation time, a weighting function $B(\varepsilon, \tau)$ is calculated:

$$B(\varepsilon, \tau) = \frac{\varepsilon(\tau - 0.5)}{(1 - \varepsilon) + (\tau - 0.5)} \tag{10}$$

The presence of solid modifies the evolution of fluid and it is incorporated into the fluid evolution equation with an additional collision term $\Omega_i^s$:

$$f_i(\boldsymbol{x} + \boldsymbol{e}_i t, t + \Delta t) = f_i(\boldsymbol{x}, t) - \frac{1}{\tau}(1 - B)\left(f_i(\boldsymbol{x}, t) - f_i^{eq}(\boldsymbol{x}, t)\right) + B\boldsymbol{\Omega}_i^s \tag{11}$$

$$\boldsymbol{\Omega}_i^s = f_{-i}(\boldsymbol{x}_i, t) - f_i(\boldsymbol{x}_i, t) + f_i^{eq}(\rho, \boldsymbol{U}_s) - f_{-i}^{eq}(\rho, \boldsymbol{U}) \tag{12}$$

where the subscript $-i$ denotes the opposite direction of $i$, $\boldsymbol{U}_s$ and $\boldsymbol{U}$ denote solid and fluid velocities at position $\boldsymbol{x}$. From the modified LBM method, the hydrodynamic force $(\boldsymbol{F}_f)$ and torque $(\boldsymbol{T}_f)$ acting on the particles can be calculated as the sum of momentum transfer across the fluid-solid boundary nodes:

$$\boldsymbol{F}_f = \sum_{j=1}^{n} \boldsymbol{B}_j \sum_{i=0}^{8} \boldsymbol{\Omega}_i^s \boldsymbol{e}_i \tag{13}$$

$$\boldsymbol{T}_f = \sum_{j=1}^{n} \left( \boldsymbol{B}_j (\boldsymbol{x}_j - \boldsymbol{x}_p) \times \sum_{i=0}^{8} \boldsymbol{\Omega}_i^s \boldsymbol{e}_i \right) \tag{14}$$

where $n$ is the total number of LBM nodes overlapped by solids; $\boldsymbol{x}_p$ center of solid particle $\boldsymbol{x}_j$ is the position of $j^{th}$ overlapped node.

## Discrete Element Method

Discrete element method (DEM) developed by Cundall and Stack (1979) is a numerical technique that deals with the simulation of granular material at individual particle scale level.

The governing behavior of particles is based on Newton's second law, and particles are considered as rigid bodies with small overlaps at the contact points, i.e., soft sphere approach. Fig. 1(b) shows a 2D representation of particle contact pair with overlap, where $r_1$ and $r_2$ are radii of particles and $r_{12}$ is the distance between the particle centers. The two particles are said to be in contact only if $r_1 + r_2 > r_{12}$. The overlapping distance is given by $\delta = (r_1 + r_2 - r_{12})$. When two particles or particle-wall come into contact, the contact forces would start acting between them. The contact forces acting between the two entities is the summation of the forces in the normal and tangential direction (Itasca 2018):

$$\boldsymbol{F}_c = \boldsymbol{F}_n\boldsymbol{n} + \boldsymbol{F}_t\boldsymbol{t} \tag{15}$$

where $\boldsymbol{F}_n$ , $\boldsymbol{F}_t$ are the normal and tangential contact forces, and $\boldsymbol{n}$, $\boldsymbol{t}$ are the unit vectors in normal and tangential directions, respectively. For a saturated granular media, the body forces and the forces due to the presence of fluid would all act together on a particulate system. Therefore, the equations of motion for a typical particle are given as:

$$m_p\boldsymbol{a} = \sum_c \boldsymbol{F}_c + \boldsymbol{F}_g + \boldsymbol{F}_f \tag{16}$$

$$I_p\dot{\boldsymbol{\omega}} = \sum_c \boldsymbol{r}_c \times \boldsymbol{F}_c + \boldsymbol{T}_f \tag{17}$$

Where $m_p$ is particle mass, $I_p$ is particle moment of inertia, $\boldsymbol{a}$ and $\boldsymbol{\omega}$ are translational acceleration and angular velocity, $\boldsymbol{F}_g$ is gravitational acceleration vector, $\boldsymbol{F}_f, \boldsymbol{T}_f$ are the force and torque applied by the fluid on the particle, $\boldsymbol{F}_c$ refers to inter-particle contact force, and $\boldsymbol{r}_c$ is a vector connecting the particle center to the contact location.

**Computational scheme**

This study developed LBM fluid code to simulate fluid flow and coupled with DEM software (PFC2D) to simulate solid particles interactions (Itasca 2018). The LBM fluid code was developed using the Python programming language. In DEM, the calculated timestep $\Delta t_{DEM}$ was chosen in such a way that it is smaller than the critical time step $\Delta t_{cr}$, and equal or smaller than the LBM time step $\Delta t_{LBM}$. Both methods work on an explicit time integration technique. Therefore, the coupling can be achieved by synchronizing the time steps and exchanging the fluid force and particle information within the DEM and LBM numerical schemes (Timm et al. 2016). Hence, $\Delta t_{LBM} = N_s \Delta t_{DEM}$, where $N_s$ is the positive integer indicating the number of sub-cycles performed in DEM for every LBM step. In this study, after precise calibration the $N_s$ value of 10 was adopted in all the simulations. It is identified that $N_s$ has a significant influence on the DEM timestep, with the decrease of $N_s$ the DEM timestep will be increased and increase of $N_s$ causes a decrease in DEM timestep. Therefore, a suitable proportionate $N_s$ value was considered in this study to balance the stability of the simulation and computational time.

## LBM-DEM model validation

### Consolidation test

Before simulating the cone penetration test (CPT) using LBM-DEM numerical model framework, the coupled LBM-DEM model was validated by performing a one-dimensional consolidation test. The system configuration and dimensions of the model ($120\, mm \times 120\, mm$) are shown in Fig. 2(a). The representative volume element with approximately 6120 particles (i.e., 2D disks) was created and the linear contact model was used for capturing particle - particle and particle - wall interactions. (Itasca 2018). The grading of the soil sample was generated based on the uniform distribution of particle sizes between 1 mm to 2 mm.

Further, this test allows determining the fluid compressibility value that controls the pore pressure response in the chamber (Johnson et al. 2017). The fluid compressibility value of

$1.88 \times 10^{-6}$ $(Pa^{-1})$ was calculated using Eq. (9). The compressibility value depends on the fluid parameters such as node spacing, relaxation parameter and fluid viscosity.

The consolidation test was performed in two stages: in the first stage, the specimen was subjected to an increase in vertical stress $(\Delta\sigma)$, and the corresponding increase in excess pore fluid pressure was evaluated in undrained conditions. In the second stage, the consolidation of the specimen was initiated by dissipating the excess pore fluid pressure.

Stage 1: After generating the particles in the chamber, the assembly was brought to an equilibrium where the specimen was under initial compressive stress $(\sigma_0)$. Then the fluid was introduced into the chamber by initiating the LBM subroutine with the aforementioned fluid compressibility value and the whole assembly was brought to an equilibrium. No-slip fluid boundary conditions were applied at the walls of the chamber. The entire system was then subjected to a vertical stress increment of 5 kPa. The response of the fluid-solid medium was evaluated in undrained conditions. The fluid response was captured by integrating the fluid pressure change within the system during the load application. The change in fluid pressure with time is demonstrated in Fig. 3(a), where the pressure increases gradually and then remains constant over time. The model captures an excess pore fluid pressure of 5 kPa, which is coherent with the increment in confining stress. The assembly's saturation state was also verified in this stage and Skempton's B value $(B = \frac{\Delta u}{\Delta\sigma})$ was found to be 1.

Stage 2: During the consolidation stage, the fluid boundary conditions at the top and bottom sides of the chamber were changed from no-slip to free-flow conditions making it a two-way drainage arrangement for dissipating the generated excess pore fluid pressure. Similarly, Fig. 3(b) shows dissipation of excess pore fluid pressure at any given time $t$. The model's dissipated pore fluid pressure response was validated with the analytical framework (Eq. 18 and 19) using the time-rate of consolidation theory proposed by Terzaghi (1925).

$$u_z = \sum_{m=0}^{m=\infty} \left[\frac{2u_0}{M}\sin\left(\frac{Mz}{H_{dr}}\right)\right] e^{-M^2 T_v} \tag{18}$$

$$T_v = \frac{c_v t}{H_{dr}^2} \tag{19}$$

Where $u_0$ is initial excess pore fluid pressure, $m$ is an integer and $M = \frac{\pi}{2}(2m+1)$, $T_v$ is the time factor, and $u_z$ is excess pore fluid pressure at time $t$. The drainage length $H_{dr}$ is considered as half of the length of the specimen because of two-way drainage conditions, and the ratio of $(\frac{z}{H_{dr}})$ becomes 1 with position $(z)$ being at the center of the specimen. The $c_v$ value was back-calculated comparing the analytical equation (Eq.18) and model prediction results (See Fig.3b). The back-calculated $c_v$ value of $0.011\ m^2 s^{-1}$ exhibits a good agreement between model prediction and the analytical equation.

## LBM - DEM simulation of the cone penetration test

### LBM-DEM model setup

The same system configuration mentioned earlier (see section 3.1) was used for performing 2D CPT simulations. The penetrometer and frictionless chamber dimensions are shown in Fig. 2(b). The ratio of chamber width to the cone diameter $(R_d = W/d)$ was chosen as 20 to minimize the radial boundary effects (Bolton et al. 1999). The frictional cone tip was modeled with an angle of 60°. During CPT, the predefined boundary conditions in calibration chambers are developed to replicate field conditions (Arroyo et al. 2011). Generally, four types of boundary conditions (BC1, BC2, BC3 and BC4) are used for cone penetration testing, as shown in Table 2. However, except BC2, all other boundary conditions develop volumetric strains during cone penetration testing and cannot be considered for simulating an undrained response. Therefore, the BC2 condition was implemented in the current study, as it is a constant volume condition. The model parameters for all the LBM-DEM simulations presented in this study are given in Table 1. A wide range of contact stiffness values was used in DEM – CPT studies ranging from $1 \times 10^5$ to $1 \times 10^9$ N/m (Jiang et al. 2006; Arroyo et al. 2011; Mcdowell et al. 2012; Ciantia et al. 2016; Khosravi et al. 2019). After a few trials of preliminary simulations of varying the stiffness parameters in the aforementioned range, the value of $1 \times 10^6$ N/m as contact stiffness was selected, as it captured a qualitative representative behavior without any numerical stability problems. It is also understood that grain-scale experimental investigations on quartz sand specimens performed by (Sandeep and Senetakis 2018a, 2018b, 2019; Sandeep et al. 2021; Reddy et al. 2022) revealed that the individual contact stiffness value between two particles at small to medium strains is in the range of $1 \times 10^5$ - $2 \times 10^6$ N/m, which further justifies the chosen DEM input parameters.

All the tests simulated in this study were subjected to confining stress $(\sigma_c)$ of $25\ kPa$, the boundary condition (BC2) was implemented by restricting the vertical, horizontal movement of chamber walls, and the system was brought to an equilibrium state. As the CPT chamber walls remain stationary throughout the simulation, the chamber rigid walls were set as bounce back boundaries with a 'No-slip' boundary condition, which represents the wall is impermeable to the fluid. In this study, the Immersed Moving Boundary (IMB) technique was employed to capture the fluid-particle, fluid-cone interactions. Based on the position of particles and cone, the fluid grid was mapped, indicating the occupancy of lattice cells by solids (particles and cone). The 'No-slip' boundary condition was implemented at the interface using the non-equilibrium bounce-back principle and the fluid evolution equation was modified according to the volume fraction occupancy of lattice cells (See Eq. 10 and 11). The interaction between cone and particle was modeled using DEM contact law. Therefore, no specific boundary condition was implemented between cone and particle.

The main parameter examined in this study is the penetration rate and its influence on the generation of excess pore pressure response and cone tip resistance. Another important phenomenon to consider while simulating higher penetration rates is maintaining a quasi-static regime during the test. It is quite possible that the high penetration rate would transform the system into a dynamic loading regime that could lead to dynamic effects. The inertial number $(I)$ can be used to characterize the quasi-static regime and has been extensively used in many DEM and CPT simulations (Janda and Ooi 2016; Khosravi et al. 2019). The inertial number is defined as $I = \dot{\varepsilon} d\sqrt{\rho/p'}$ , where, $\dot{\varepsilon}$ is shear strain rate, $p'$ is mean effective stress, $d$ is mean particle size, and $\rho$ is particle density. In cone penetration, the shear strain rate is defined as $\dot{\varepsilon} = v_{cone}/6r_{cone}$. The shear strain rate is dependent on the penetration rate and the width of the yield zone in the chamber. In general, in DEM-CPT simulations, the width of the yield zone is defined as six times the radius of the cone (Janda and Ooi 2016). Janda and Ooi (2016) reported that during CPT tests, the inertia number should be less than $(I < 10^{-2})$ to represent a quasi-static condition. Herein, the same condition was taken as a reference. The width of the yield zone is considered based on the literature (Janda and Ooi 2016). And it is mainly chosen to calculate the inertial number to ensure the system is in quasi-static equilibrium. The recent analytical study of CPT on sands by Ahmadi and Dariani (2017) highlights that the yield zone is mainly affected by the relative density and applied stresses on the soil. Nevertheless, the penetration rate and the nature of the soil can also perhaps influence the formation of the yield zone in the cone penetration problems. However, this requires further experimental and numerical studies in terms of vertical/horizontal stress responses and pore pressure evolution across the chamber.

Generally, the laboratory CPT studies on sands at standard penetration rate (20 mm/s) and at lower rates (< 20 mm/s) are considered as a drained condition. Therefore, no excess pore pressure response was reported in the literature (Pournaghiazar et al. 2013; Kluger et al. 2021).

Nonetheless, in this study, the penetration rate in the range of 20 – 200 mm/s was selected to capture the excess pore pressure during the cone penetration under undrained conditions. The various cone penetration rates considered in this study are 20 mm/s, 50 mm/s, 75 mm/s, 100 mm/s, 150 mm/s, and 200 mm/s. For all the mentioned rates, the inertial number was less than $10^{-2}$, thereby ensuring that all the simulations presented in this work were under quasi-static loading conditions. To model the cone surface as 'perfectly rough' and to have a uniform frictional resistance in the entire chamber, the same particle-particle interface friction coefficient value of 0.3 was considered in the study between the cone-particle. A similar approach was followed in previous DEM modeling of CPT studies, where the same friction coefficient value was adopted between cone-particle and particle-particle interactions (Jiang et al. 2006; Arroyo et al. 2011; Mcdowell et al. 2012; Butlanska et al. 2013; Falagush et al. 2015; Ciantia et al. 2016). Depending on the penetration rate used in the simulations, the computational time varied between 10 days to four weeks for each simulation on Intel(R) Xeon(R) CPU 6136 @3GHz processor.

## Cone penetration test results

Fig. 4(a - f) shows the cone resistance $(\mathrm{q_t})$ and excess pore fluid pressure $(\Delta\mathrm{u})$ responses measured for different penetration rates against the depth of penetration. It is evident from fig 4(a) that the cone resistance (raw data) is fluctuating, and this type of response was reported in previous DEM – CPT studies (e.g., Butlanska et al. 2013; Ciantia et al. 2016), where this behavior is observed because of low $n_p$ value. In this study, the ratio of cone diameter to mean particle size $(n_p = d/d_{50})$ is 4. The fluctuations in the data are filtered out by fitting the raw data to the expression reported by Arroyo et al. (2011): $q_t(z) = a(1 - e^{-bz})$. Where $a$ and $b$ are fitting parameters, z is depth. Parameter $a$ refers to the asymptotic value, $b$ refers to 95% of depth where asymptotic value is reached, thus $z_{95} = 3/b$. Thereby, a smooth cone resistance profile was extracted from the raw data, which represents the model response. The typical cone resistance against depth in the standard penetration rate condition, along with the filtered data, is shown in Fig. 4(a). Whereas for the remaining test cases, only the filtered cone resistance ($q_t$) and excess pore fluid pressure response ($\Delta u$) with depth (z) are presented in Fig. 4. Initially, the $q_t$ increases with z and reaches a steady-state condition at z = 50 mm (after eight times the cone's diameter). A similar evolution of ($q_t$) has been observed for all different penetration rates. The LBM-DEM model predictions of steady-state cone resistances obtained at different penetration rates considered in this analysis are shown in Fig. 5(a). The solid symbols are the model data, and the dashed line represents the linear trend line of the simulation results against the penetration rates. From Fig. 5(a), it can be noticed that an increase in penetration rates have an insignificant influence on $q_t$. This observation is consistent with the experimental results reported on saturated sands by Silva and Bolton (2004) and Juran and Tumay (1989).

The excess pore fluid pressure ($\Delta u$) was measured individually at each fluid node as the cone penetrates, excluding the nodes covered by solid particles and a penetrometer (Han and Cundall 2013; Timm et al. 2016). Therefore, the excess pore pressure response shown in Fig. 4 is the average pressure of all nodes present in the pores in the undrained condition simulation setup. It is evident from Fig. 4 that the coupled model has captured the variation of excess pore fluid pressure similar to the laboratory experiments (Kim et al. 2008). The pore fluid pressure evolution during CPT is consistent with depth regardless of the penetration rate. The excess pore fluid pressure ($\Delta u$) gradually increases and reaches a steady state at depth z =50 mm (after eight times the cone's diameter). The excess pore fluid pressure generation during CPT increases with penetration rates. Overall, from Fig. 4, it is clear that the penetration rate can significantly influence the generation of excess pore fluid pressure during CPT. The increase in excess pore pressure is attributed to the fluid pressure gradients created by the cone in the fluid system based on the penetration rate. Hence, the maximum pore fluid pressure was generated in the high penetration rate condition and minimum in low penetration rate condition.

Fig. 5(b) shows the model's predicted excess pore fluid pressure with the penetration rate, along with the calibration chamber-based CPT tests on sand-clay mixtures reported by Kim et al. (2008). The laboratory experiments were conducted on 82% sand and 18% clay mixture, and the penetration rates were in the range of $0.02 - 20\ mm/s$. It is understood that the high magnitudes of excess pore pressure in the experiments may be due to the clay content. From Fig. 5(b), it can be observed that the current LBM-DEM model has qualitatively captured the increase in excess pore pressure with an increase in penetration rate, reflecting a similar trend as experiments.

### Particle displacements and fluid velocity

Fig. 6 (a), (c), (e) shows representative particle displacements and Fig. 6 (b), (d), (f) shows fluid velocity contours for a penetration rate of 200 mm/s at various depths ($z$ = 20, 40 and 60 mm), respectively. From Fig. 6(a), (c), (e), it is clear that large particle displacements have occurred around the cone tip and the sleeve area. The displacement experienced by the particles increases with the penetration depth and gradually becomes stable over depth (after about crossing the depth of 50 mm). This stability in displacement can be observed in cone resistance evolution shown in Fig. 4, where the cone resistance increases with the depth and reaches a steady-state response.

As the cone penetrates, it triggers particle displacement within the chamber and more predominantly around the cone. As a result, low-pressure zones are formed behind the particle's position in the fluid system. Therefore, a fluid pressure gradient develops in the system as the penetration depth increases and is proportional to the penetration rate. As the penetration rate increases, the particle displacements increase, leading to large-fluid pressure gradients within the chamber. These pressure gradients generate fluid flow streams across the chamber. As the fluid moves from the high-pressure zone to the low-pressure zone, the fluid flow direction is oriented upwards resisting the cone penetration. The enlarged view of the spatial distribution of fluid velocity around the penetrometer is shown in Fig. 6(g). The fluid velocity is maximum in the vicinity of the penetrometer, which is coherent with the maximum particle displacement. The fluid velocity generated in the chamber also increases with depth and reaches a constant velocity over depth. This entire phenomenon is reflected in the pore fluid pressure evolution presented in Fig 4, where the pore fluid pressure increases to a certain depth and then remains stable over depth.

The fluid velocity contours of different penetration rate conditions 100 mm/s and 20 mm/s at depth (z = 60 mm) are shown in Fig. 7(a) and (b). From the figures, it is understood that the chamber's fluid velocity depends on the penetration rate. As the penetration rate decreases, the chamber's pressure gradient decreases, resulting in reduced fluid velocity. This behavior can be seen in the excess pore fluid pressure responses shown in Fig. 4, where the pore fluid pressure generated in the chamber decreased with the penetration rate.

### Excess pore fluid pressure distribution

To illustrate the influence of particle displacements on the pore fluid pressure generation within the chamber, a line diagram plot of pressure fluctuations across the chamber is shown in Fig. 8. The schematic representation of layers marked along with the depth of the chamber, around the sleeve area and below the cone area at three different penetration depths z = 20 mm, 40 mm, and 60 mm, are shown in Fig. 8(a), (b), (c), respectively. The excess pore fluid pressure distribution across the horizontal distance of the chamber has been plotted in Fig. 8(d), (e), (f) for penetration rate condition of 200 mm/s, at three different penetration depths z = 20 mm, 40 mm, and 60 mm, respectively. The normalized horizontal distance ($X$) was calculated based on the LBM node position along the x-direction ($X = \frac{x_i - x_c}{x_c}$), where $x_i$ is the x-position of the i$^{th}$ node in that particular layer and $x_c$ is the center of the chamber. This plot provides an insight into the pore fluid pressure distribution in the chamber, especially below the cone tip and along the sleeve length. As shown in Fig. 8(d), (e), (f), at each respective penetration depth (z), the maximum pore fluid pressure was observed exactly below the cone tip (X = 0) region and above the cone shoulder position. However, the pore fluid pressure decreases with the distance away from the cone in both directions (X > 0 and X < 0) regardless of vertical position in the chamber. Concurrently, at (X = 0) position, the pore fluid pressure decreases as we move away from the cone tip in the vertical direction.

A similar trend was observed in the pore fluid pressure distribution around the sleeve area at different depths. The maximum pore fluid pressure was recorded adjacent to the penetrometer (on either side of the sleeve) and as the position moves upwards along the sleeve at z = 30 mm and z = 5 mm (see Fig. 8 (e) & (f)), the pore fluid pressure decreases. Overall, this behavior can be understood through the particle displacement and fluid velocity contours shown earlier (see Fig. 6 and 7). The fluid velocity and particle displacement are dominant around the penetrometer compared to other areas in the chamber. Therefore, the maximum pore fluid pressure was recorded in the vicinity of the penetrometer and the minimum pore fluid pressure at the ends of the chamber.

Correspondingly, at same three different penetration depths (z = 20 mm, 40 mm, 60 mm) the pore fluid generation for 100 mm/s and 20 mm/s conditions are shown in the Fig. 9 (a), (b), (c) and Fig 9(d), (e), (f), respectively. A similar phenomenon was observed in other penetration rate conditions. The particle displacements generated in the chamber are proportional to the penetration rate. Consequently, as the penetration rate decreased, the pore fluid pressure generated in the chamber also decreased.

### Evolution of fluid force

The fluid force evolution during the test has been calculated using the LBM relation (Eq. 13) for three penetration rates (20, 100, 200 mm/s), shown in Fig. 10. The fluid force evolution for only three test cases has been plotted. It can be noticed from Fig. 10 that the evolution pattern of fluid force during the test remained consistent with all the penetration rates. Linear incremental behavior has been observed until the shallow depth region (about two times the cone's diameter, z = 12 mm). After that, the fluid force reaches a steady state with minimal oscillations and remains constant along with the depth. It is understood that with an increase in the penetration rate, the fluid force acting on the particles also increases. Moreover, this behavior is due to the evolution of fluid velocity ($\boldsymbol{U}$), which is the critical parameter in LBM simulations (Eq. 12). The maximum fluid velocity was recorded for high penetration rate conditions (see Fig. 6(f) and 7), leading to high fluid force generation. With the decrease in the penetration rate the fluid velocity in the chamber also decreased, resulting in the reduction of fluid force being imposed on particles.

### Excess pore fluid pressure in histogram plots

Fig. 11(a) shows the schematic representation of the semi-circular area with different radii around the cone profile. The radius of each semi-circular area is 1r, 6r and 12r (r = cone radius). The pore pressure distribution around the cone in different positions at various depths for a penetration rate of 20 mm/s are shown in Fig. 11(b) – (j). It can be seen from Fig. 11(c), (d) that at the shallow depth region, i.e., at 20 mm, the excess pore pressure distribution was random in 6r and 12r positions. The maximum was recorded exactly beneath the cone and at shoulder positions. This behavior can be due to the non-uniform development of pressure gradients at positions away from the cone. However, this phenomenon has changed after crossing the shallow depth region. Due to the steady growth of pressure gradient across the positions, the pore pressure has been generated evenly in vertical and radial directions (see Fig. 11(e) − (j)). The Fourier series approximation equation below can capture the overall distribution trend in all the positions and best approximate the pore pressure evolution in this 2D analysis. This approximation is a two-term Fourier series with a higher fundamental frequency.

$$\frac{\Delta u(\theta)}{\Delta u_{avg}} = \left(1 + u_p \, cos \, 4\left(\theta - \theta_f\right)\right) \tag{20}$$

where $\Delta u_{avg}$ is average excess pore pressure in the divided segments, $u_p$ is the parameter describing the randomness in the distribution, and $\theta_f$ is the direction of the maximum pore pressure. Note the overall evolution of excess pore pressure remained the same for different penetration rates.

## Fabric anisotropy during CPT

The effect of penetration rate on the evolution of fabric anisotropy during the cone penetration is presented in Fig. 12. The material anisotropy with penetration depth was captured in two regions of the chamber: cone region and boundary region. Fig. 12(a) shows the schematic representation of two regions inside the chamber. The cone region is the area around the penetrometer and the boundary region is the area at the boundary surface (away from the penetrometer). The anisotropy of the material is defined as the measure of preferential orientations of the particles during the deformation (O’Sullivan 2011). Two approaches are used in this study to interpret the contacts orientations: the fabric tensor approach and the curve-fitting approach to histogram plots.

*The fabric tensor approach*: The fabric tensor is defined from the contact information data, which takes a second-order symmetric tensor form. The eigenvectors of the tensor will give the preferential orientation of the contacts and eigenvalues will quantify the magnitude of the anisotropy. The tensorial notation of the fabric tensor  is given below:

$$\emptyset_{ij} = \frac{1}{N_c}\sum_{k=1}^{N_c} n_i^k\, n_j^k \tag{21}$$

where $n_i^k$ is the unit vector describing the contact normal orientation and $N_c$ is number of contacts in the system. In a 2D analysis, Eq. 21 becomes a two-dimensional matrix with the elements being $\emptyset_{11}, \emptyset_{12}, \emptyset_{21}, \emptyset_{22}$. In this analysis, $\emptyset_{11}$ represents horizontal (X – direction) and $\emptyset_{22}$ vertical (Z – direction). The eigenvalues $(\emptyset_1, \emptyset_2)$ and their difference $(\emptyset_1 - \emptyset_2)$ gives the magnitude of the anisotropy.

*Curve fitting to histogram plots*: The polar histogram plots are commonly used to visualize the distribution of contacts orientation. By fitting a Fourier series approximation curve to the distribution data, the anisotropy of the fabric and the preferential contacts orientation can be determined. The Fourier series approximation equation used by Rothenburg and Bathurst (1989) is given below:

$$E(\theta) = \frac{1}{2\pi}[1 + a\cos2(\theta - \theta_a)] \tag{22}$$

Fig. 12(b), (c), (d) and 12(e), (f), (g) shows the evolution of fabric tensor components: $(\emptyset_{11}, \emptyset_{22})$, anisotropy $(\emptyset_1 - \emptyset_2)$ determined by Eq. 22 in the cone region and away region, respectively, for three penetration rate conditions. It can be seen that in the 'cone region' the fabric component $(\emptyset_{22})$ has the highest value in all the penetration rate conditions, indicating that the contact orientations are predominantly vertical. Whereas, in the 'away region' the component $(\emptyset_{11})$ has dominated in all the conditions indicating the preferential orientation of contacts in the horizontal direction. Moreover, the magnitude of anisotropy $(\emptyset_1 - \emptyset_2)$ in both the regions is in the range of 0.01 - 0.02. The evolution pattern remained consistent throughout the depth in all the conditions showing that the penetration rate does not affect the fabric anisotropy.

The histogram plots have not shown any variation in the representation of contacts orientations with penetration rates. So for brevity, only the typical polar histogram plots in the standard penetration rate condition (20 mm/s) representing contact orientations in the cone and boundary regions are shown in Fig. 13(a) and (b), respectively. In the cone region, as the $(\emptyset_{22})$ component was dominant indicating the vertical direction that phenomenon can be seen in Fig. 13(a), where the principal direction of fabric anisotropy being $\theta_a = 128^{\circ}$. Correspondingly, in the boundary region the $(\emptyset_{11})$ component domination representing the horizontal direction is seen in Fig. 13(b), with the principal direction of the anisotropy around $\theta_a = 10^{\circ}$. Similar observations of anisotropy behavior in 2D space during CPT have been reported by Paniagua et al. (2018).

## Conclusions

In this study, a 2D LBM-DEM coupled model was employed to simulate the penetration rate effect in the cone penetration test (CPT). The fluid was modeled using LBM and coupled to DEM software (PFC2D). One dimensional consolidation test was first simulated for calibrating the soil-fluid interactions. The results obtained from the 1D consolidation test simulation showed good agreement with the analytical equation solution and demonstrated the potential of LBM in capturing the excess pore fluid pressure during loading.

The CPT simulations were performed at various cone penetration rates using the coupled LBM-DEM model. The model has captured a steady state cone resistance and excess pore fluid pressure response for all penetration rate conditions. The excess pore fluid pressure was found to increase with an increase in the penetration rate adopted. However, the penetration rates influence on the cone resistance was found to be insignificant. The excess pore fluid pressure generated during the CPT with the increase in penetration rate was consistent with the laboratory calibration chamber studies carried out by Kim et al. (2008). It was observed that the particles close to the cone move along with the cone contributing to the overall deformation during CPT. The displacement of particles during cone penetration developed low-pressure zones resulting in the pressure gradient in the fluid system. With increase in the penetration rate, the particle displacements also increased, leading to large-fluid pressure gradients across the chamber. The excess pore fluid pressure generated in the chamber is directly proportional to the penetration rate. Therefore, the maximum pore fluid pressure was generated in the high penetration rate condition and minimum in the low penetration rate condition.

The excess pore pressure distribution along the normalized horizontal distance in the chamber emphasized that the maximum pore fluid pressure was generated exactly below the cone region and over the cone shoulder position. Regardless of penetration depth in the chamber, the excess pore fluid pressure decreases with the distance away from the cone in both directions. The fluid force evolution during the test has shown that the magnitude of the fluid force generated in the chamber is directly proportional to the penetration rate. Similar to the excess pore fluid pressure response, the fluid force generated in the chamber increased as the penetration rate increased. In addition, the excess pore fluid pressure histogram plots have shown a non-uniform pore fluid pressure generation at shallow depths in the areas away from the cone. However, this phenomenon has changed after crossing the shallow depth region, a uniform pore fluid generation was observed in vertical and radial directions. The magnitude of fabric anisotropy was in the range of 0.01 - 0.02 throughout the depth. Around the cone area, the fabric component ($\emptyset_{22}$) has dominated in all the penetration rate conditions indicating that the contact orientations were predominantly vertical. Likewise, away from the cone, the component ($\emptyset_{11}$)

has dominated in all the conditions representing the preferential orientation of contacts was horizontal direction.

Overall, the simulation results have shown that the LBM-DEM model can efficiently simulate the cone penetration test and capture the cone-particle-fluid interactions. Even though the 2D LBM-DEM simulations have captured the pore pressure generation during CPT testing, a 3D coupled LBM DEM model will provide a more realistic behavior and additional insights into the pore pressure and cone resistance responses.

## Limitations

It is understood that there are robust contact models available in DEM to analyze the contact deformations and certainly a realistic particle shape (polygonal) can be generated in the DEM assembly for analyzing the soil response. However, implementing them in large-scale problems like the CPT test would be computationally very demanding. In addition, simulating a saturated soil response with fluid presence will still increase the computational time many folds. Therefore, it is critical to focus on simulation using a non-linear Hertz-Mindlin (H-M) contact model with realistic particle shapes. In addition, the influence of material parameters such as contact stiffness, inter-particle friction, cone-particle friction on the macroscopic responses needs to be investigated in future studies.

The high penetration rates in sands significantly influence the excess pore fluid pressures but have no considerable impact on cone resistance $q_t$. This may be due to the viscous effect as well. The authors acknowledge that the viscous effects are present at high penetration rates, and its influence on the results has not been considered in this study. Therefore, simulations should be extended to capture the effect of viscosity and its impact on the CPT results.

## Data availability

Some or all data, models or code generated or used during the study are available from the corresponding author upon reasonable request. These data include the DEM input files to set up the particle assembly, LBM – DEM coupling code and the simulation results used to generate all figures.

## Acknowledgment

The authors acknowledge the assistance of all university partners (University of Western Australia (lead university), University of New South Wales, University of South Australia, and University of Wollongong) involved in this project. This work is part of the TAILLIQ (Tailings Liquefaction) project, an Australian Research Council (ARC) Linkage Project supported by Anglo American, BHP, Freeport-McMoRan, Newmont, Rio Tinto, and Teck.

# References

Ahmadi, M. M., and Dariani, A. G. 2017. “Cone penetration test in sand: A numerical-analytical approach.” *Computers and Geotechnics*. 90: 176-189.

American Society for Testing and Materials. 2012. “Standard test method for electronic friction cone and piezocone penetration testing of soils.” *ASTM International*

Arroyo, M., Butlanska. J, Gens. A, Calvetti. F, and Jamiolkowski. M. 2011. “Cone penetration tests in a virtual calibration chamber.” *Géotechnique.* 61(6): 525-531.

Bhatnagar, P.L., Gross. E.P, and Krook. M. 1954. “A Model for Collision Processes in Gases. I. Small Amplitude Processes in Charged and Neutral One-Component Systems.” *Physical Review.* 94(3): 511-525.

Butlanska, J., Arroyo. M, Gens. A, and O’Sullivan. C. 2013. “Multi-scale analysis of cone penetration test (CPT) in a virtual calibration chamber.” *Canadian Geotechnical Journal.* 51(1): 51-66.

Butlanska, J., Arroyo. M, and Gens. A. 2010. “Virtual calibration chamber cpt on ticino sand.” *In 2nd International Symposium on Cone Penetration Testing*.

Bolton, M.D., Gui. M.W, Garnier. J, Corte. J.F, Bagge. G, and Laue. J. 1999. “Centrifuge cone penetration tests in sand.” *Géotechnique.* 49(4): 543-552.

Boutt, D.F., Cook. B.K, and Williams. J.R. 2011. “A coupled fluid–solid model for problems in geomechanics: application to sand production.” *International Journal for Numerical and Analytical Methods in Geomechanics.* 35(9): 997-1018.

Ciantia, M.O., Arroyo. M, Butlanska. J, and Gens. A. 2016. “DEM modelling of cone penetration tests in a double-porosity crushable granular material.” *Computers and Geotechnics.* 73: 109-127.

Chapman, G. A. 1979. “The interpretation of friction cone penetrometer tests in sand.” Doctoral dissertation, Monash University.

Cook, B., Noble. D, and Williams. J. 2004. “A direct simulation method for particle-fluid systems.” *Engineering Computations.* 21(2-3): 151-168.

Cui, X., Li. J, Chan. A, and Chapman. D. 2014. “Coupled DEM–LBM simulation of internal fluidization induced by a leaking pipe.” *Powder Technology.* 254(299-306).

Cundall, P.A., and Strack. O.D.L. 1979. “A discrete numerical model for granular assemblies.” *Géotechnique*. 29(1): 47-65.

DeJong, J.T., and Randolph. M. 2012. “Influence of partial consolidation during cone penetration on estimated soil behavior type and pore pressure dissipation measurements.” *Journal of Geotechnical and Geoenvironmental Engineering*, 138(7): 777-788.

Ecemis, N., and Bakunowicz. P. 2018. “Feasible packing of granular materials in discrete-element modelling of cone-penetration testing.” *Geomechanics and Geoengineering.* 13(3): 198-216.

El Shamy, U., and Abdelhamid. Y. 2014. “Modeling granular soils liquefaction using coupled lattice Boltzmann method and discrete element method.” *Soil Dynamics and Earthquake Engineering.* 67(119-132).

Falagush, O., McDowell. G.R, and Yu. H.S. 2015. “Discrete Element Modeling of Cone Penetration Tests Incorporating Particle Shape and Crushing.” *International Journal of Geomechanics.* 15(6): 04015003.

Feng, Y.T., Han. K, and Owen. D.R.J. 2007. “Coupled lattice Boltzmann method and discrete element modelling of particle transport in turbulent fluid flows: Computational issues.” *International Journal for Numerical Methods in Engineering.* 72(9): 1111-1134.

Han, Y., and Cundall. P.A. 2013. “LBM–DEM modeling of fluid–solid interaction in porous media.” *International Journal for Numerical and Analytical Methods in Geomechanics.* 37(10): 1391-1407.

He, X., and Luo. L.S. 1997. “Lattice Boltzmann Model for the Incompressible Navier–Stokes Equation.” *Journal of Statistical Physics*. 88(3-4): 927-944.

Huang, A.B., and Ma. M.Y. 1994. “An analytical study of cone penetration tests in granular material.” *Canadian Geotechnical Journal.* 31(1): 91-103.

Huang, X., Hanley, K. J., O'Sullivan, C., and Kwok, C. Y. 2014. “Exploring the influence of interparticle friction on critical state behavior using DEM.” *International Journal for Numerical and Analytical Methods in Geomechanics*. *38*(12): 1276-1297.

Indraratna, B., Phan. N.M, Nguyen. T.T, and Huang. J. 2021. “Simulating Subgrade Soil Fluidization Using LBM-DEM Coupling.” *International Journal of Geomechanics*, 21(5): 04021039.

Itasca Consulting Group, Inc. 2018. “PFC - Particle Flow Code, Ver. 6.0.” *Minneapolis: Itasca.*

Janda, A., and Ooi. J.Y. 2016. “DEM modeling of cone penetration and unconfined compression in cohesive solids.” *Powder Technology.* 293: 60-68.

Jaeger, R.A., DeJong. J.T, Boulanger. R.W, Low. H.E, and Randolph. M.F. 2010. “Variable penetration rate CPT in an intermediate soil.” *In Proceedings of the International Symposium on Cone Penetration Testing.*

Jiang, M.J., Yu. H.S, and Harris. D. 2006. “Discrete element modelling of deep penetration in granular soils.” *International Journal for Numerical and Analytical Methods in Geomechanics.* 30(4): 335-361.

Jiang, M., Dai. Y, Cui. L, Shen. Z, and Wang. X. 2014. “Investigating mechanism of inclined CPT in granular ground using DEM.” *Granular Matter.* 16(5): 785-796.

Johnson, D.H., Vahedifard. F, Jelinek. B, and Peters. J.F. 2017. “Micromechanics of undrained response of dilative granular media using a coupled DEM-LBM model: A case of biaxial test.” *Computers and Geotechnics.* 89: 103-112.

Juran, I., and Tumay, M. T. 1989. “Soil stratification using the dual pore-pressure piezocone test.” *Transportation Research Record*. *1235*: 68-78.

Kasyap, S. S., and Senetakis, K. 2019. “Interface load–displacement behavior of sand grains coated with clayey powder: Experimental and analytical studies.” *Soils and Foundations*. *59*(6): 1695-1710.

Khosravi, A., Martinez. A, and DeJong. J.T. 2019. “DEM simulations of CPT measurements and soil classification.” *Canadian Geotechnical Journal.* 57(9): 1369-1387.

Kim, K., Prezzi. M, Salgado. R, and Lee. W. 2008. “Effect of Penetration Rate on Cone Penetration Resistance in Saturated Clayey Soils.” *Journal of Geotechnical and Geoenvironmental Engineering*. 134(8): 1142-1153.

Kinloch, H., and O'Sullivan. C. 2007. “A micro-mechanical study of the influence of penetrometer geometry on failure mechanisms in granular soils.” *In Advances in Measurement and Modeling of Soil Behavior.* 1-11.

Kluger, M.O., Kreiter. S, Stähler. F.T, Goodarzi. M, Stanski. T, and Mörz. T. 2021. “Cone penetration tests in dry and saturated Ticino sand.” *Bulletin of Engineering Geology and the Environment*, 80(5): 4079-4088.

Lu, Q., Randolph. M.F, Hu. Y, and Bugarski. I.C. 2004. “A numerical study of cone penetration in clay.” *Géotechnique.* 54(4): 257-267.

Lunne, T., Powell. J.J, and Robertson. P.K. 2002. “Cone penetration testing in geotechnical practice.” *CRC Press*.

Mahmoodzadeh, H., Boylan, N., Randolph, M., and Cassidy, M. 2011. “The effect of partial drainage on measurements by a piezoball penetrometer.” *International Conference on Offshore Mechanics and Arctic Engineering*. 44397: 1007-1016.

Mcdowell, G.R., Falagush. O, and Yu. H.S. 2012. “A particle refinement method for simulating DEM of cone penetration testing in granular materials.” *Géotechnique Letters.* 2(3): 141-147.

Mollon, G., Quacquarelli, A., Andò, E., and Viggiani, G. (2020). “Can friction replace roughness in the numerical simulation of granular materials?.” *Granular Matter*. *22*(2): 1-16.

Nadimi, S., Otsubo, M., Fonseca, J., and O’Sullivan, C. 2019. “Numerical modelling of rough particle contacts subject to normal and tangential loading.” *Granular Matter*. *21*(4): 1-14.

Noble, D.R., and Torczynski. J.R. 1998. “A lattice-Boltzmann method for partially saturated computational cells.” *International Journal of Modern Physics C.* 9(08): 1189-1201.

Obrzud, R. F., Truty, A., and Vulliet, L. 2011. “Numerical modeling and neural networks to identify model parameters from piezocone tests: I. FEM analysis of penetration in two-phase continuum." *International Journal for Numerical and Analytical Methods in Geomechanics*. *35*(16): 1703-1730.

Otsubo, M., O'Sullivan, C., Hanley, K. J., and Sim, W. W. 2017. "The influence of particle surface roughness on elastic stiffness and dynamic response." *Géotechnique*. *67*(5): 452-459.

Owen, D.R.J., Leonardi. C.R, and Feng, Y.T. 2011. "An efficient framework for fluid–structure interaction using the lattice Boltzmann method and immersed moving boundaries." *International Journal for Numerical Methods in Engineering.* 87(1-5): 66-95.

O'Sullivan, C. 2011. *Particulate discrete element modelling: a geomechanics perspective.* CRC Press.

Paniagua, P., Fonseca. J, Gylland. A, and Nordal. S. 2018. "Investigation of the change in soil fabric during cone penetration in silt using 2D measurements." *Acta Geotechnica*, 13(1): 135-148.

Pournaghiazar, M., Russell. A.R, and Khalili. N. 2013. "The cone penetration test in unsaturated sands." *Géotechnique*. 63(14): 1209-1220.

Ramsey, N., 2010. "Some issues related to applications of the CPT". In *2nd International Symposium on Cone Penetration Testing, CPT* (Vol. 10).

Randolph, M.F., Hope, S.F. 2004. "Effect of cone velocity on cone resistance and excess pore pressures.": *Engineering Practice and Performance of Soft Deposits*. 147-152.

Reddy, N. S., He, H., and Senetakis, K. 2022. "DEM analysis of small and small-to-medium strain shear modulus of sands." *Computers and Geotechnics*. *141*: 104518.

Rothenburg. L., and Bathurst. R.J. 1989. "Analytical study of induced anisotropy in idealized granular materials." *Geotechnique*, 39(4): 601-614.

Sandeep, C. S., and Senetakis, K. 2018a. "Effect of Young's modulus and surface roughness on the inter-particle friction of granular materials." *Materials*. 11(2): 217.

Sandeep, C. S., & Senetakis, K. 2018b. "Grain-scale mechanics of quartz sand under normal and tangential loading." *Tribology International*. 117: 261-271.

Sandeep, C. S., & Senetakis, K. 2019. "An experimental investigation of the microslip displacement of geological materials." *Computers and Geotechnics*. 107: 55-67.

Sandeep, C. S., Li, S., & Senetakis, K. 2021. "Experimental and analytical investigation on the normal contact behavior of natural proppant simulants." *Geomechanics and Geophysics for Geo-Energy and Geo-Resources*, 7(4): 1-15.

Schneider, J.A., Lehane, B.M., and Schnaid, F. 2007. "Velocity effects on piezocone measurements in normally and over consolidated clays." *International Journal of Physical Modelling in Geotechnics*, *7*(2): 23-34.

Senetakis, K., Anastasiadis, A., and Pitilakis, K. 2012. "The small-strain shear modulus and damping ratio of quartz and volcanic sands." *ASTM International*.

Senetakis, K., Anastasiadis, A., and Pitilakis, K. 2013. “Normalized shear modulus reduction and damping ratio curves of quartz sand and rhyolitic crushed rock.” *Soils and Foundations*. *53*(6): 879-893.

Sheng, D., Kelly, R., Pineda, J., and Bates, L. 2014. “Numerical study of rate effects in cone penetration test.” *3rd international symposium on cone penetration testing*. 419-428.

Silva, M.F., and Bolton. M.D. 2004. “Centrifuge penetration tests in saturated layered sands.” *In Proceedings of 2nd International Conference on Site Characterization.*

Sitharam, T. G., and Vinod, J. S. 2010. “Evaluation of shear modulus and damping ratio of granular materials using discrete element approach.” *Geotechnical and Geological Engineering,* 28(5): 591-601.

Suzuki, Y. 2015. “Investigation and interpretation of cone penetration rate effects.” Doctoral dissertation, University of Western Australia.

Terzaghi, K., 1925. “Erdbaumechanik auf bodenphysikalischer Grundlage.” *F. Deuticke*.

Timm, K., Kusumaatmaja. H, Kuzmin. A, Shardt. O, Silva. G, and Viggen. E. 2016. *The lattice Boltzmann method: principles and practice.* Springer International Publishing AG Switzerland, ISSN: 1868-4521.

Van der Poel, J.T. and Schenkeveld, F.M. 1998. “A preparation technique for very homogenous sand models and CPT research.” *Centrifuge*. 149 – 154.

Yi, J.T., Goh. S.H, Lee. F.H, and Randolph. M.F. 2012. “A numerical study of cone penetration in fine-grained soils allowing for consolidation effects.” *Géotechnique*. 62(8): 707-719.

Yang, G.C., Jing. L, Kwok. C.Y, and Sobral. Y.D. 2019. “A comprehensive parametric study of LBM-DEM for immersed granular flows.” *Computers and Geotechnics.* 114: 103100.

Yang, Z. X., Yang, J., and Wang, L. Z. 2012. “On the influence of inter-particle friction and dilatancy in granular materials: a numerical analysis.” *Granular matter*. *14*(3): 433-447.

Zou, Q., and He. X. 1997. “On pressure and velocity boundary conditions for the lattice Boltzmann BGK model.” *Phys Fluids.* 9(6): 1591–1598.

# Tables

Table 1:

Model parameters used for DEM-LBM simulations

| *Parameter* | *Value* |
|---|---|
| Normal stiffness of boundaries $k_n$ $(N\ m^{-1})$ | $7.5 \times 10^7$ |
| Tangential stiffness of boundaries $k_s$ $(N\ m^{-1})$ | $5 \times 10^7$ |
| Normal stiffness of particles $k_n$ $(N\ m^{-1})$ | $1 \times 10^6$ |
| Tangential stiffness of particles $k_s$ $(N\ m^{-1})$ | $1 \times 10^6$ |
| Particle density $(kg\ m^{-3})$ | 2650 |
| Inter planar void ratio | 0.17 |
| Inter particle friction coefficient | 0.3 |
| Cone-particle friction coefficient | 0.3 |
| Fluid viscosity $(m^2\ s^{-1})$ | $1 \times 10^{-4}$ |
| Fluid density $(kg\ m^{-3})$ | 1000 |
| Lattice spacing $\Delta x$ $(m)$ | 0.000075 |
| Relaxation parameter (τ) | 0.6 |
| LBM time step $\Delta t_{LBM}$ (s) | $1.88 \times 10^{-6}$ |
| DEM time step $\Delta t_{DEM}$ (s) | $1.88 \times 10^{-7}$ |

Table 2:

Typical CPT boundary conditions used in calibration chambers

| *Boundary condition* | *Horizontal direction* | *Vertical direction* |
|---|---|---|
| BC1 | Stress = constant | Stress = constant |
| BC2 | Strain = 0 | Strain = 0 |
| BC3 | Strain = 0 | Stress = constant |
| BC4 | Stress = constant | Strain = 0 |

# Figures

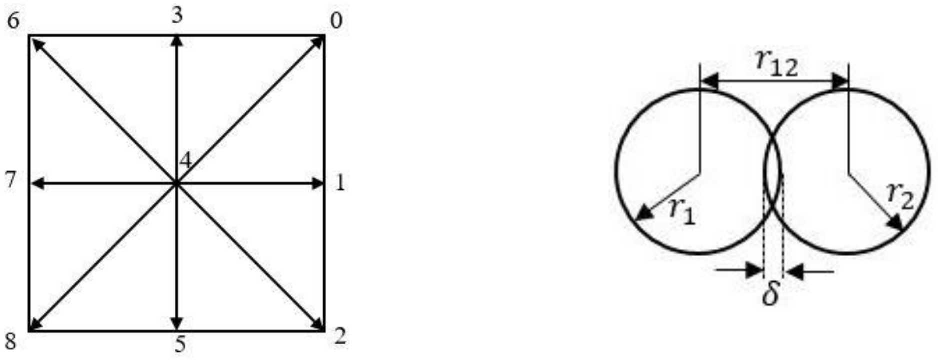

(a) (b)

Fig. 1. (a) D2Q9 lattice structure for 2D LBM with 9 lattice directions. (b) Schematic representation of contacts between particles in DEM.

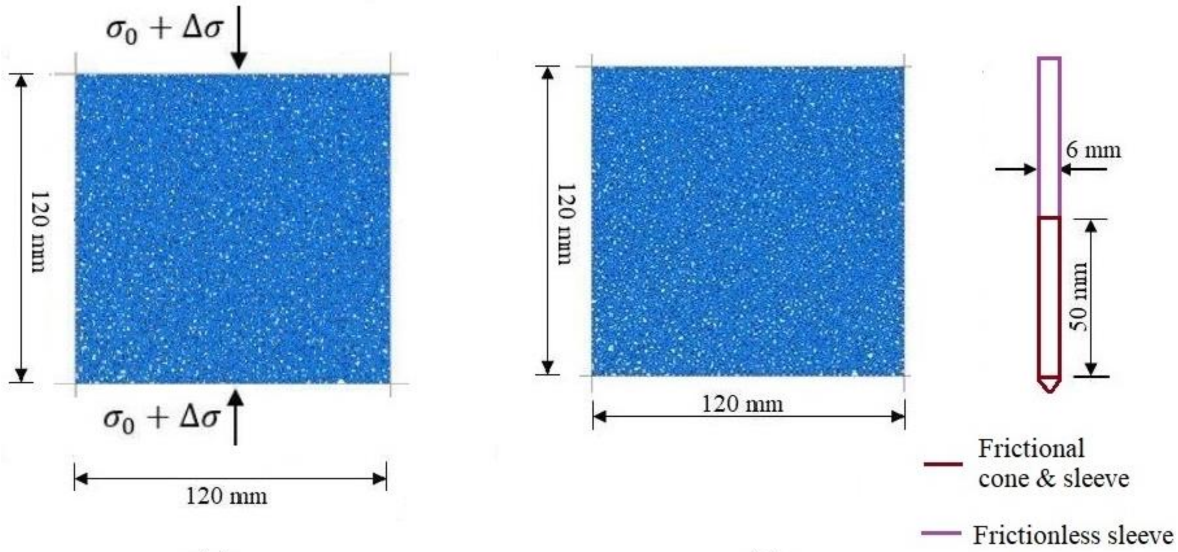

(a) (b)

Fig. 2. (a) Simulation configuration and dimensions of consolidation test and (b) Cone penetration test. where $\sigma_0$ is initial compressive stress and $\Delta\sigma$ is an increase in external applied stress.

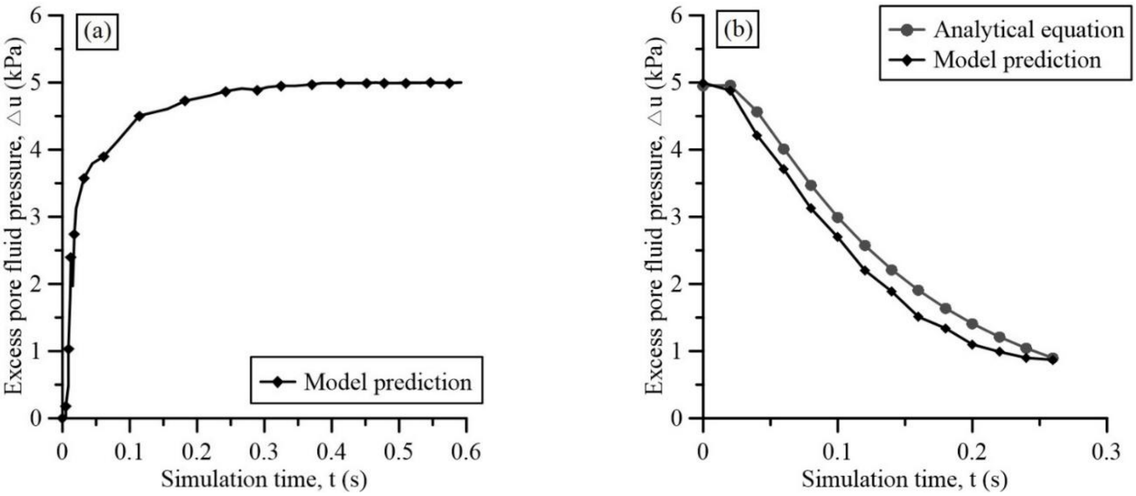

Fig. 3. Results from the consolidation test: (a) Excess pore fluid pressure rise in the loading stage where $\Delta\sigma = 5\ kPa$ (b) Dissipation of excess pore fluid pressure and comparison with the analytical solution

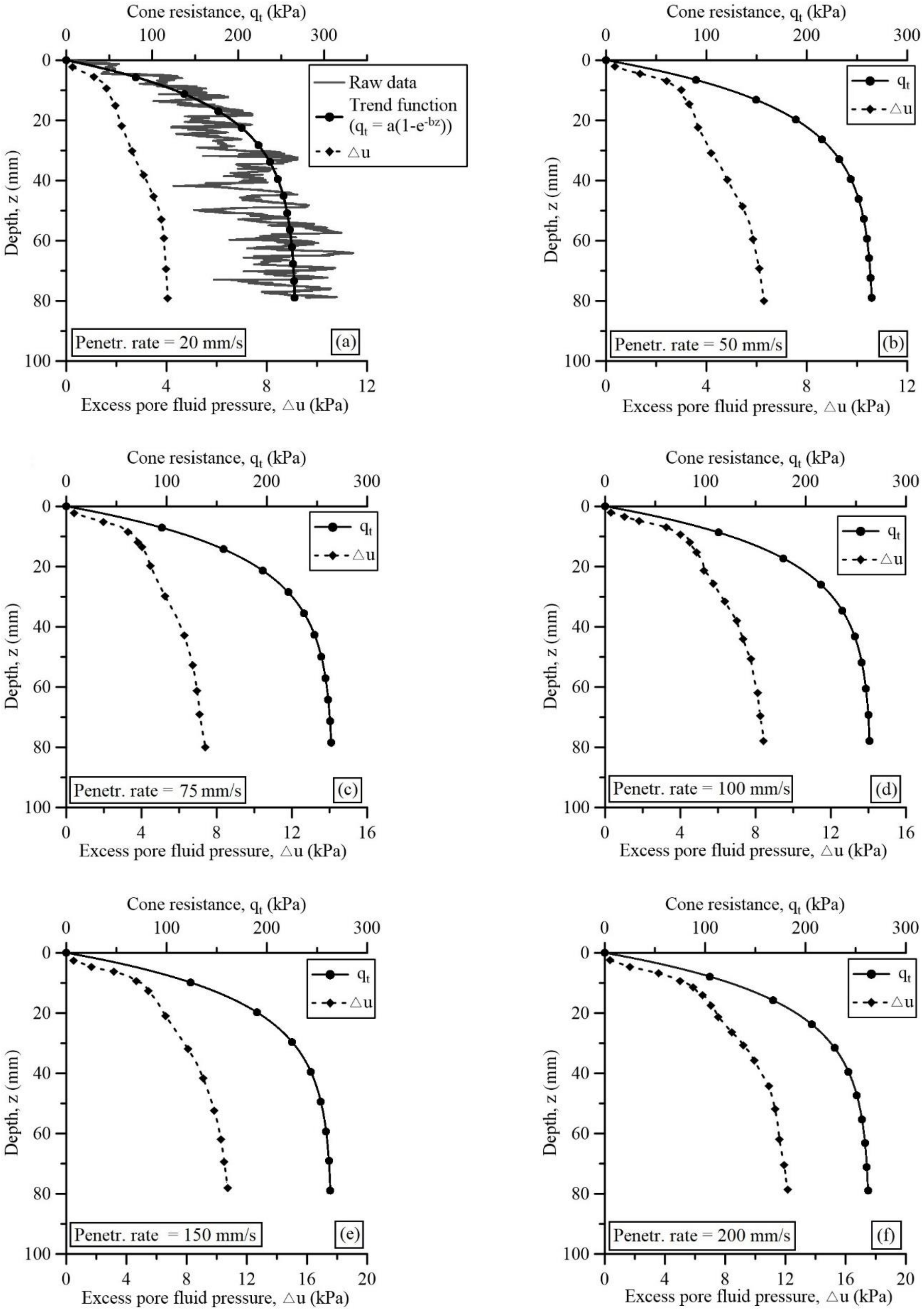

Fig. 4 (a) – (f). Results of tip resistance and pore fluid pressure against the depth of penetration for various penetration rates

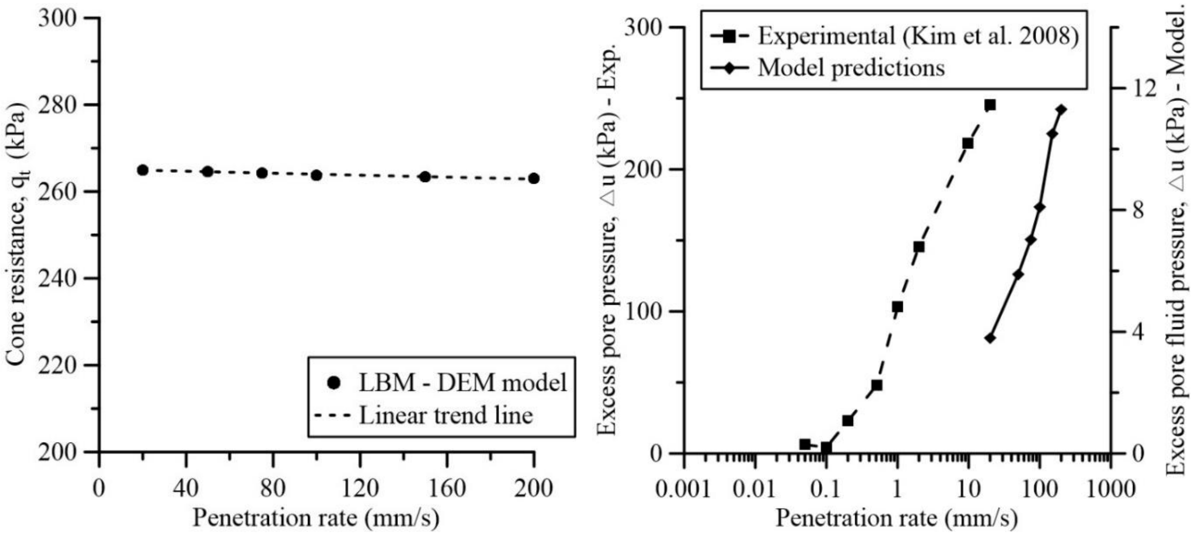

(a) (b)

Fig. 5. (a) Model predictions of steady-state cone resistance at different penetration rates considered in this analysis. (b) Comparison of model's pore fluid pressure responses with experimental results at different penetration rates

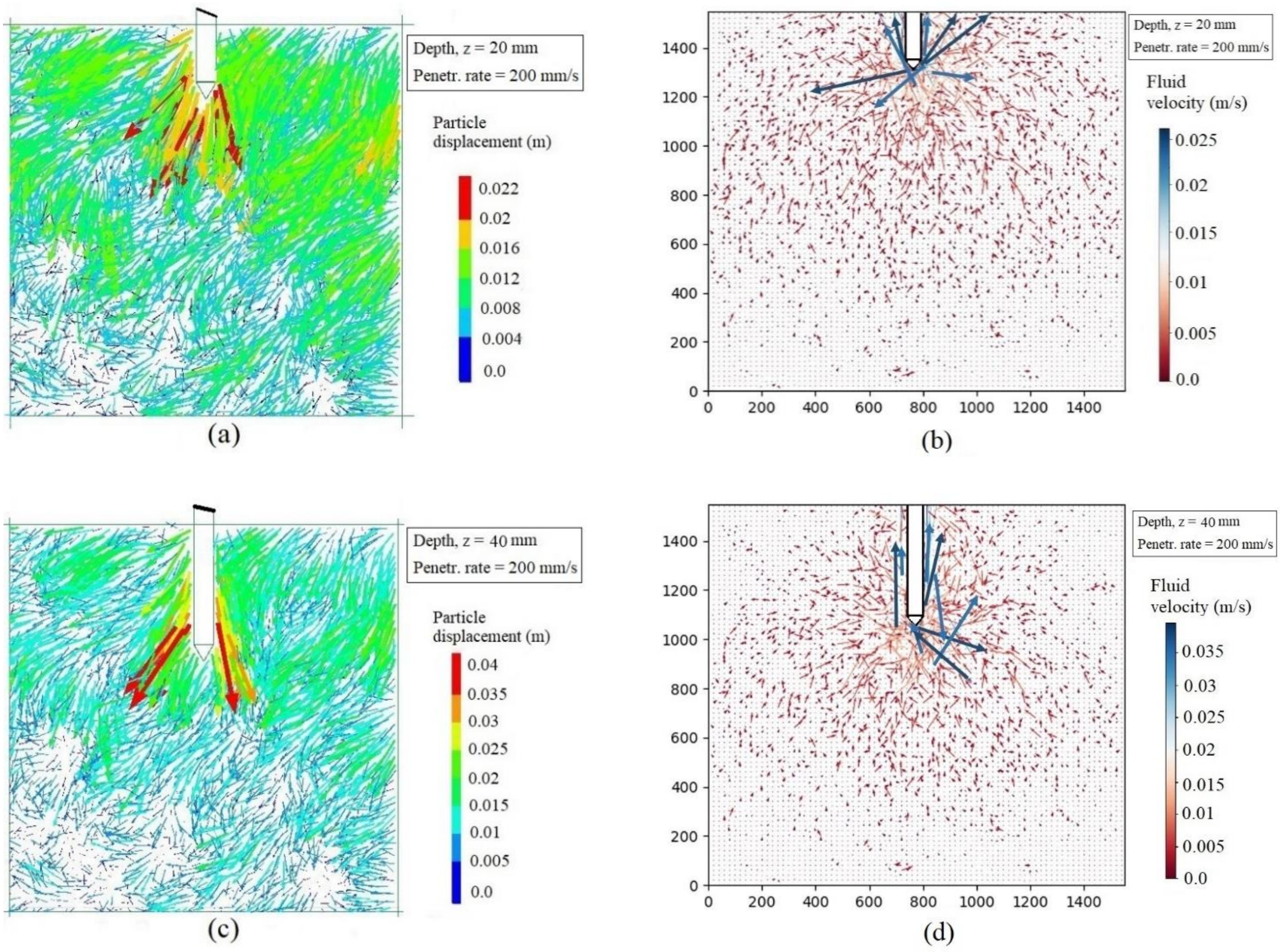

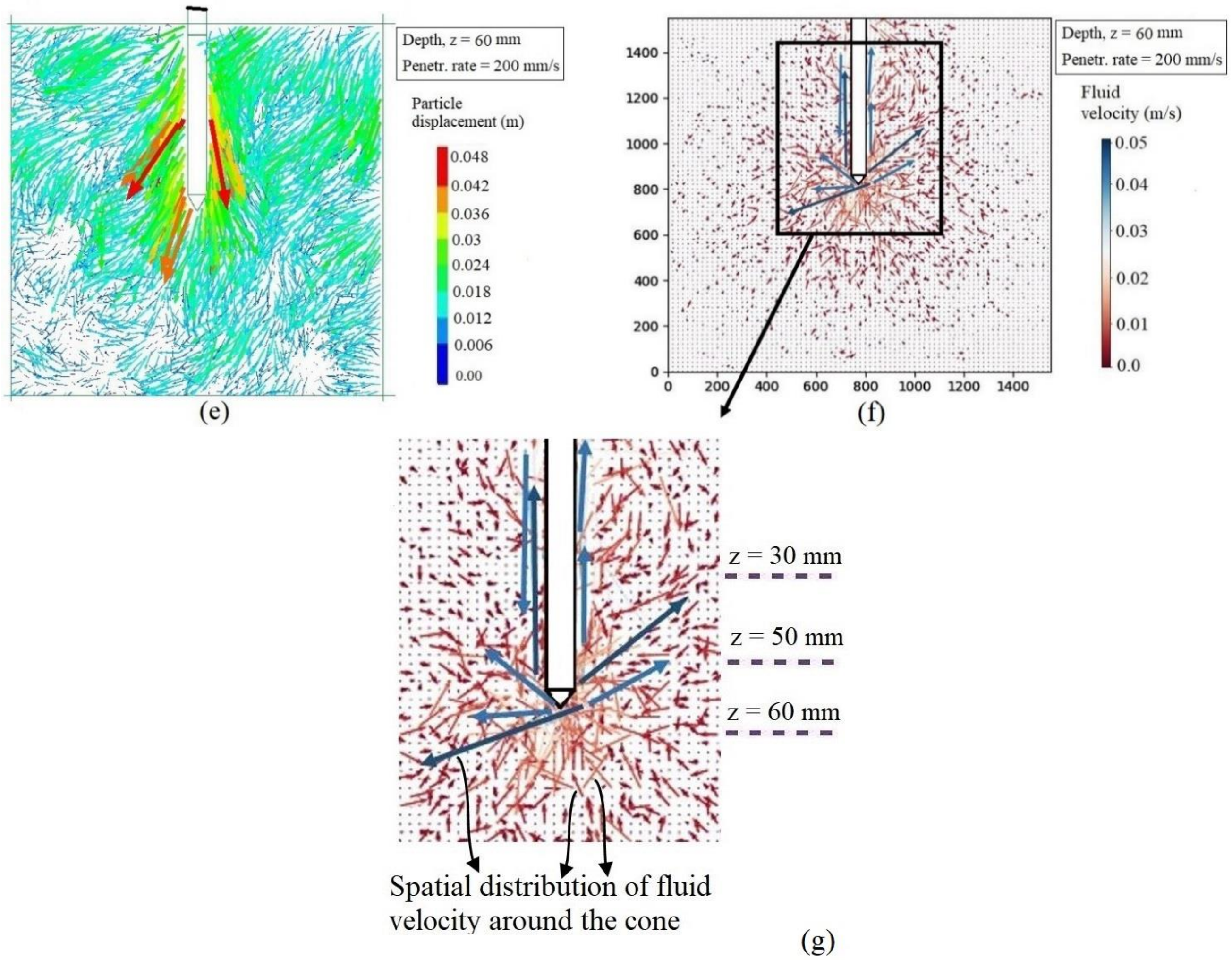

(e) (f)

Spatial distribution of fluid velocity around the cone

(g)

Fig. 6(a) – (f). Particle displacement vectors and Fluid velcity (stream line plot) contours during CPT simulation at different depths with the penetration rate of 200 mm/s. Fig 6(g). The enlarged view shows the spatial distribution of the fluid velocity around the penetrometer.

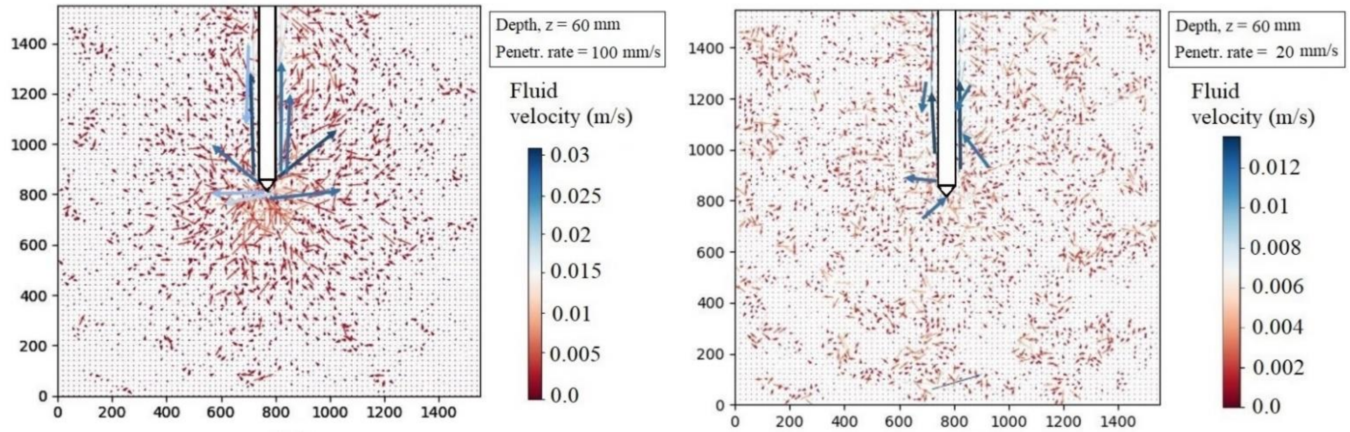

(a) (b)

Fig. 7(a), (b). Fluid velocity (stream line plot) contours at depth z = 60 mm with penetration rate of 100 mm/s, and 20 mm/s

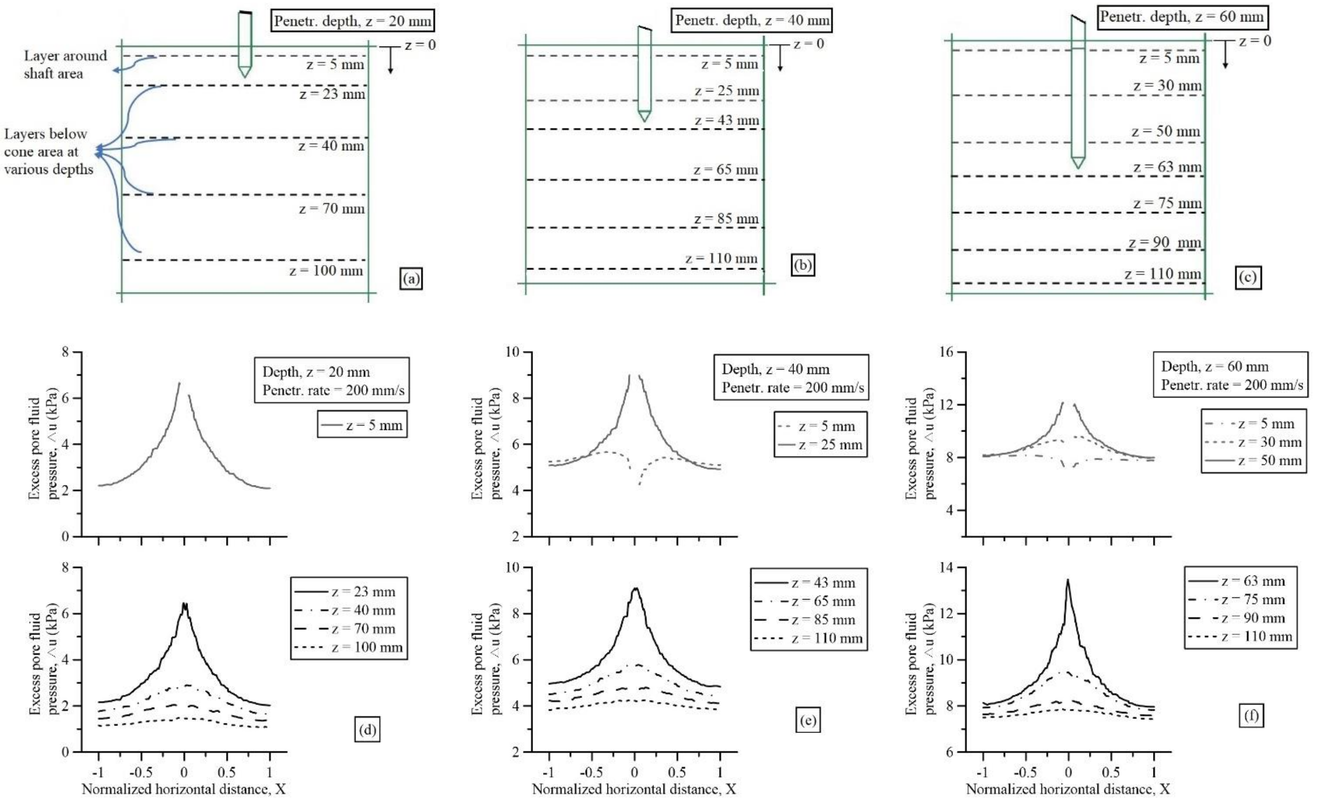

Fig. 8(a), (b), (c) shows the schematic representation of layers marking along with the chamber's depth around shaft area and below the cone area at three different penetration depths z = 20 mm, 40 mm, and 60 mm, respectively. Fig. 8(d), (e), (f) pore fluid pressure distribution along the normalized horizontal distance at three respective penetration depths in the penetration rate condition of 200 mm/s.

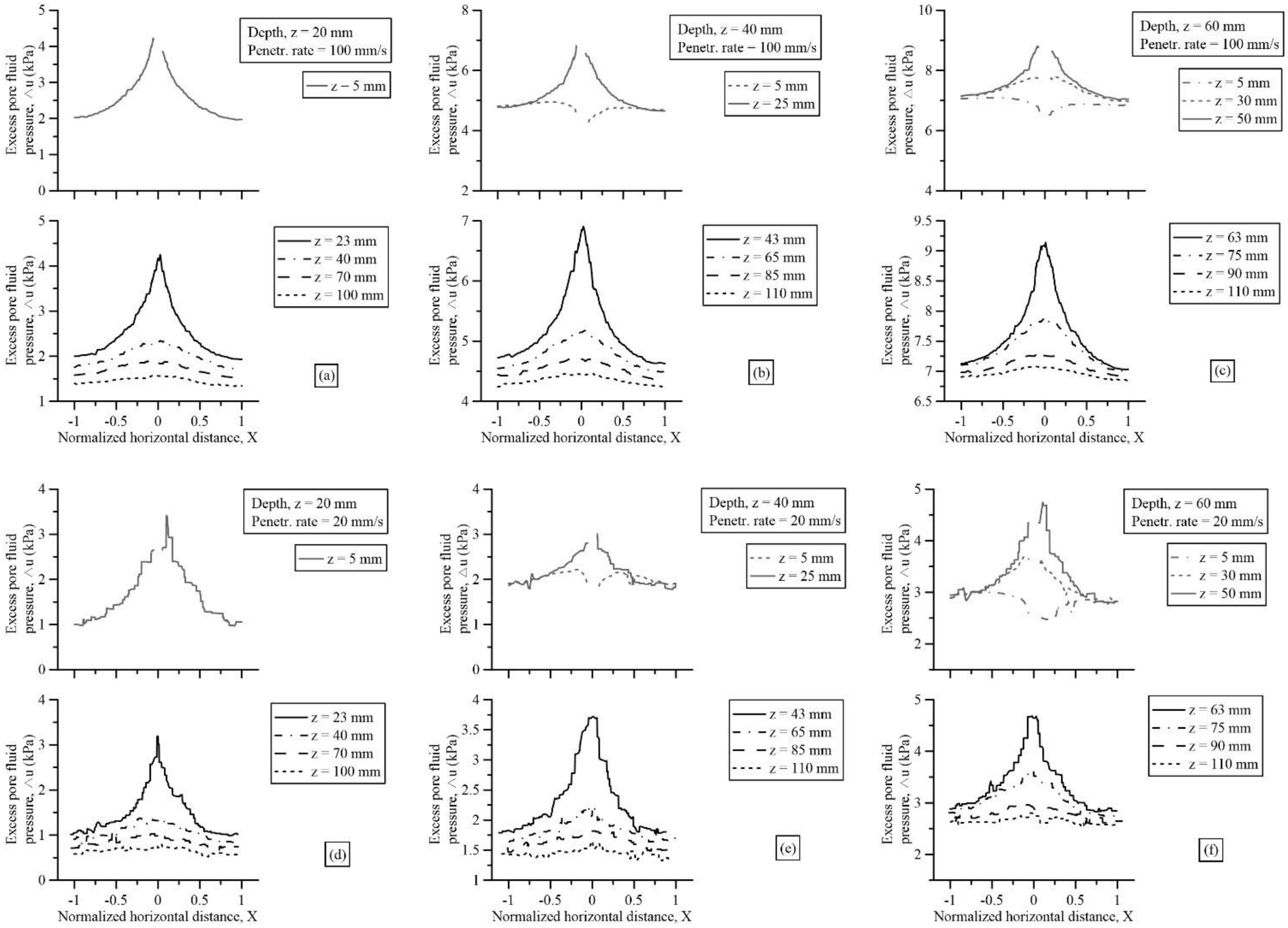

Fig. 9(a), (b), (c) and (d), (e), (f) pore fluid pressure distribution along the normalized horizontal distance at three respective penetration depths in the penetration rate condition of 100 mm/s and 20 mm/s, respectively.

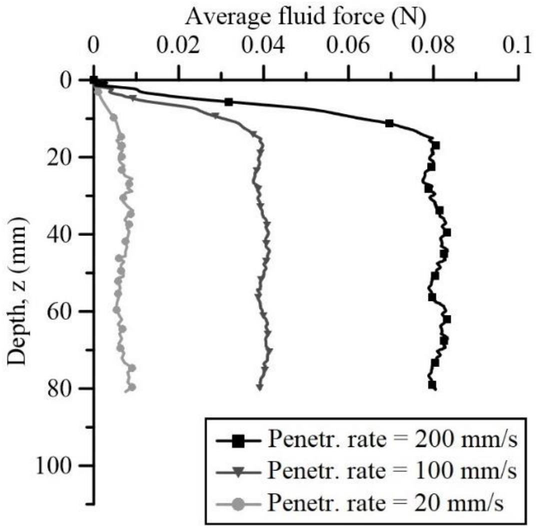

Fig. 10. Fluid force evolution during the test using the LBM relation for three penetration rates (20, 100, 200 mm/s).

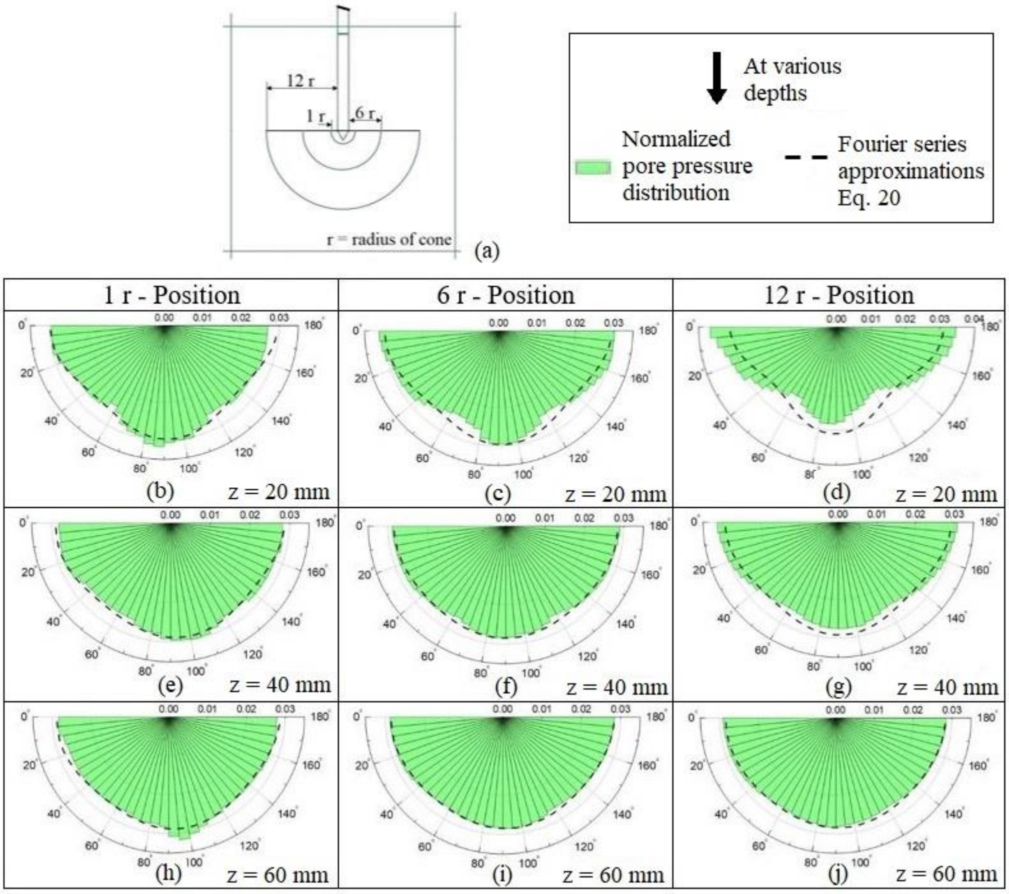

Fig. 11(a). Schematic representation of the semi-circular zones with different radii around the cone profile. Fig. 11(b) - (j) Histogram plots of pore pressure distribution around the cone profile referring to the different radius of the zones at various depths for a penetration rate condition of 20 mm/s.

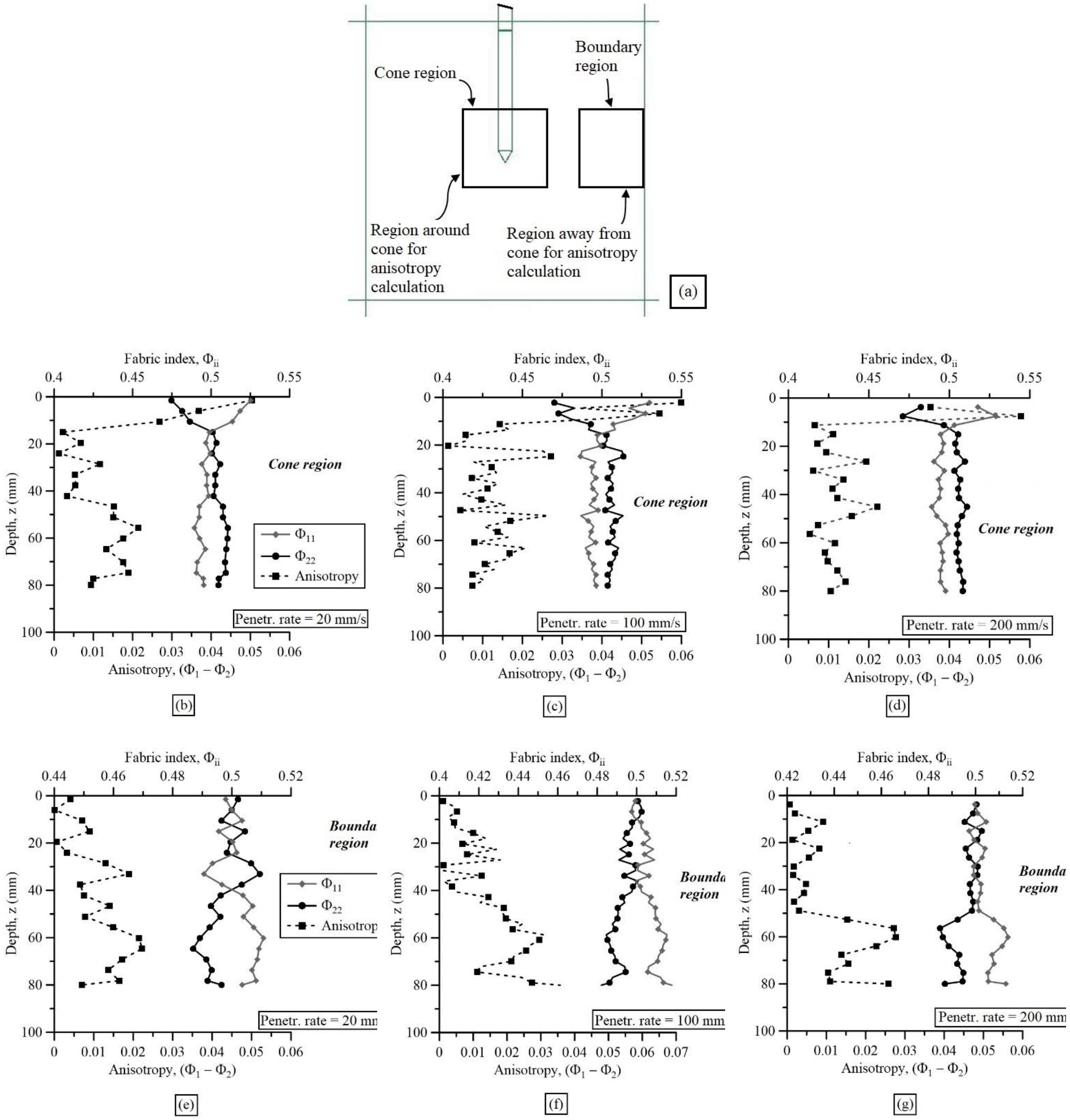

Fig. 12(a) schematic representation of regions inside the chamber 'cone region' and 'boundary region'. Fig. 12. (b) (c) (d) shows the evolution of fabric tensor components in the cone region and Fig. 12 (e) (f) (g) shows the evolution of fabric tensor components in the boundary region: for three penetration rates (20, 100, 200 mm/s).

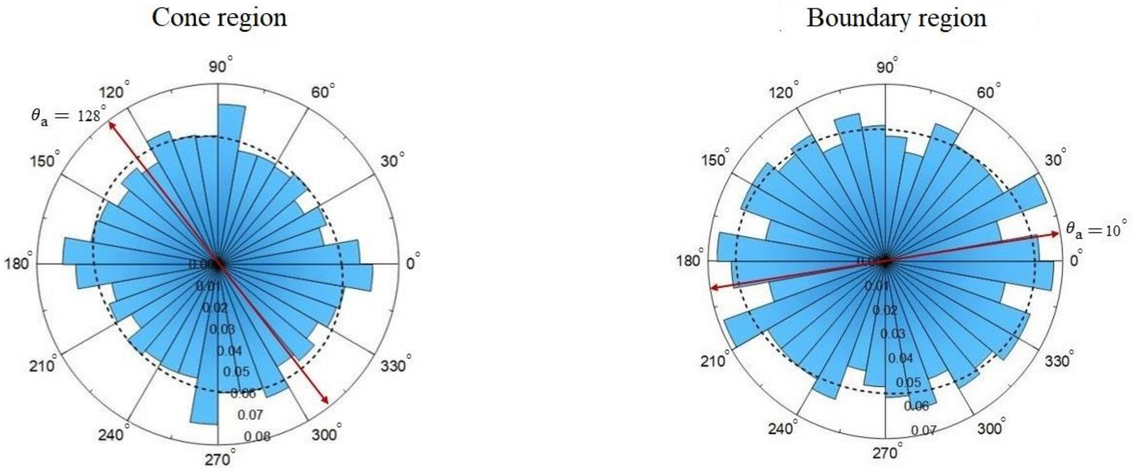

(a) (b)

Fig. 13(a) and (b) Typical polar histogram plots representing contact orientations in the cone and boundary regions for a penetration rate condition of 20 mm/s.